# Supplementary Information

# Interfacial alloying between lead halide perovskite crystals and hybrid glasses

Li et al.

**This PDF file includes:**

Supplementary Table 1

Supplementary Figs.1 to 37

**Supplementary Table 1. Results of the extended X-ray absorption fine structure (EXAFS) fitting for $(CsPbI_3)_{0.40}(a_gZIF\text{-}62)_{0.60}$ composites before and after 350°C sintering for Zn K and Pb $L_3$ edge.**

| Name | Coordination number (CN) | Bond length | Sintering | R-factor |
|---|---|---|---|---|
| Zn-N | 5.07±0.26 | 1.99±0.004 | Before | 0.007 |
| Zn-C | 6.96±1.35 | 3.02±0.018 | Before | 0.007 |
| Pb-O | 3.27±0.35 | 2.46±0.007 | Before | 0.005 |
| Pb-I | 1.69±0.16 | 3.13±0.011 | Before | 0.005 |
| Zn-N | 5.04±0.31 | 1.98±0.005 | After | 0.007 |
| Zn-C | 4.59±1.10 | 2.99±0.020 | After | 0.007 |
| Pb-I | 6.80±1.23 | 3.12±0.042 | After | 0.010 |
| Pb-Zn | 4.08±0.47 | 1.80±0.013 | After | 0.010 |

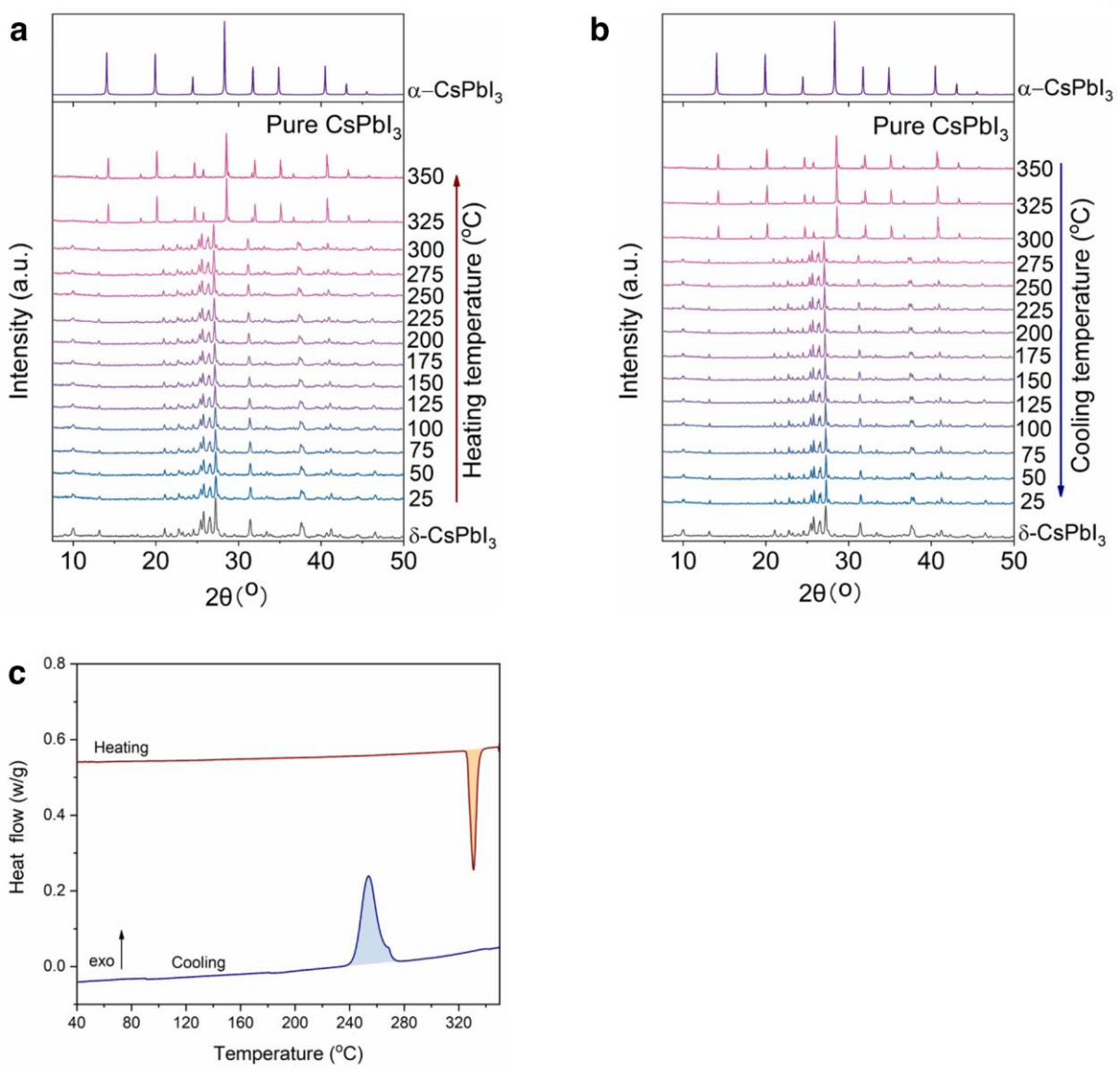


**Supplementary Fig. 1. Phase transition of the pure $CsPbI_3$. a** *In-situ* XRD pattern for pure $CsPbI_3$ during the heating process. **b** *In-situ* XRD pattern for pure $CsPbI_3$ during the cooling process. **c** DSC results for pure $CsPbI_3$ for heating and cooling ramps. Data was collected under constant flowing nitrogen protection (20 mL/min). The tempertaure ramping rate were 20 and 10 ℃/min during the heating and cooling process, respectively.

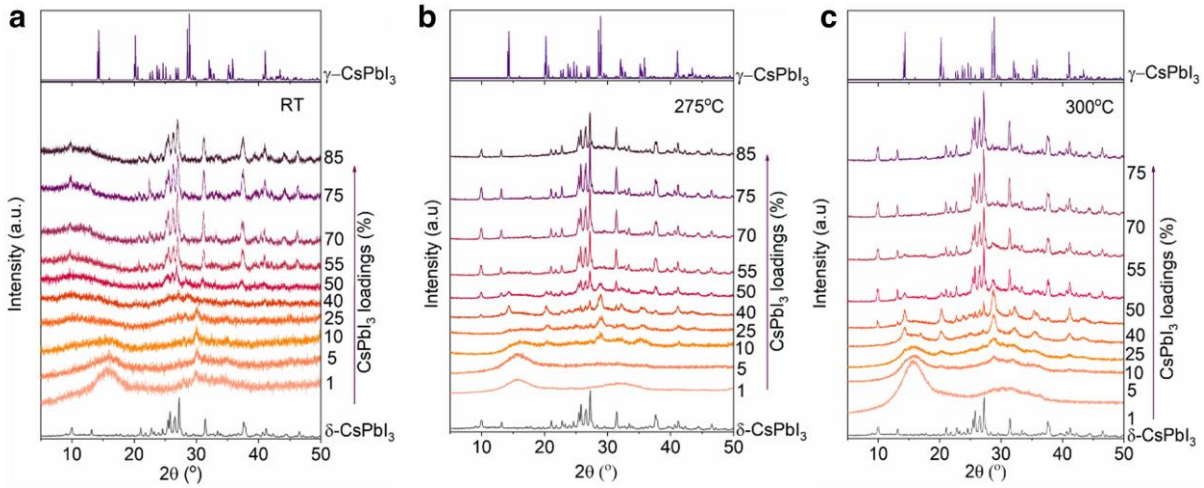


**Supplementary Fig. 2. Crystal structures of the composites with different components and sintered under different temperatures. a** *Ex-situ* XRD pattern of ($CsPbI_3$) ($a_g$ZIF-62) (X/Y), and ($CsPbI_3$)$_X$($a_g$ZIF-62)$_Y$ composites prepared at **b** 275 ℃ and (c) 300 ℃ sintering.

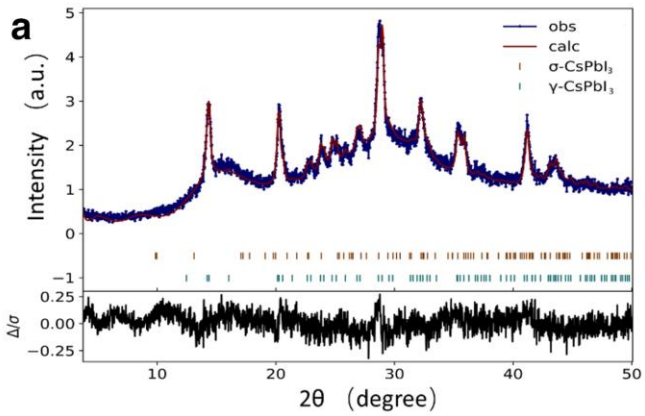


| Lattice parameters | Lattice parameters reported in ref. | Lattice parameters | Lattice parameters reported in ref. |
|---|---|---|---|
| a=10.3822 Å | a=10.4500(5) Å | a=8.6232 Å | a=8.6198(6) Å |
| b=4.8068 Å | b=4.7965(2) Å | b=8.8085 Å | b=8.8518(6) Å |
| c=17.7523 Å | c=17.7602(8) Å | c=12.4534 Å | c=12.5012(7) Å |
| α=90° | α=90° | α=90° | α=90° |
| β=90° | β=90° | β=90° | β=90° |
| γ=90° | γ=90° | γ=90° | γ=90° |
| V=885.929 Å$^3$ | V=890.20(7) Å$^3$ | V=945.920 Å$^3$ | V=953.852(11) Å$^3$ |
| Space group: *Pnma* | | Space group: *Pbnm* | |
| Crystal system: Orthorhombic (σ) | | Crystal system: orthorhombic (γ) | |
| Weight faction: 0 (sig: 0.0078) | | Weight faction: 100% (sig: 0.0078) | |
| $R_{wp}$=8.074% | | | |

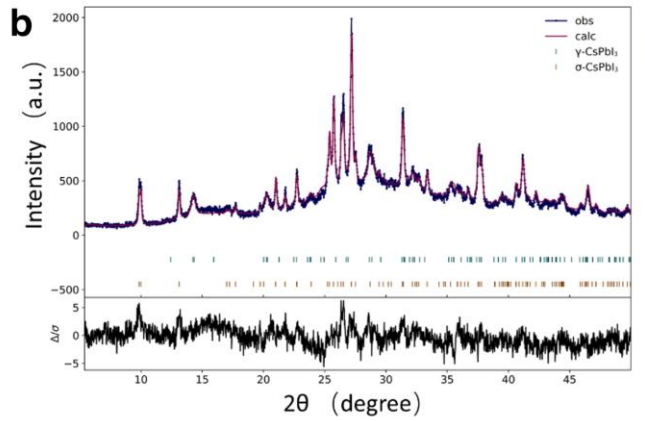


| Lattice parameters | Lattice parameters reported in ref. | Lattice parameters | Lattice parameters reported in ref. |
|---|---|---|---|
| a=10.4382 Å | a=10.4500(5) Å | a=8.7326 Å | a=8.6198(6) Å |
| b=4.7884 Å | b=4.7965(2) Å | b=8.8679 Å | b=8.8518(6) Å |
| c=17.7395 Å | c=17.7602(8) Å | c=12.3619 Å | c=12.5012(7) Å |
| α=90° | α=90° | α=90° | α=90° |
| β=90° | β=90° | β=90° | β=90° |
| γ=90° | γ=90° | γ=90° | γ=90° |
| V=888.665 Å$^3$ | V=890.20(7) Å$^3$ | V=957.306 Å$^3$ | V=953.852(11) Å$^3$ |
| Space group: *Pnma* | | Space group: *Pbnm* | |
| Crystal system: Orthorhombic (σ) | | Crystal system: orthorhombic (γ) | |
| Weight faction: 71.31% (sig: 0) | | Weight faction: 28.69% (sig: 0) | |
| $R_{wp}$=9.171% | | | |

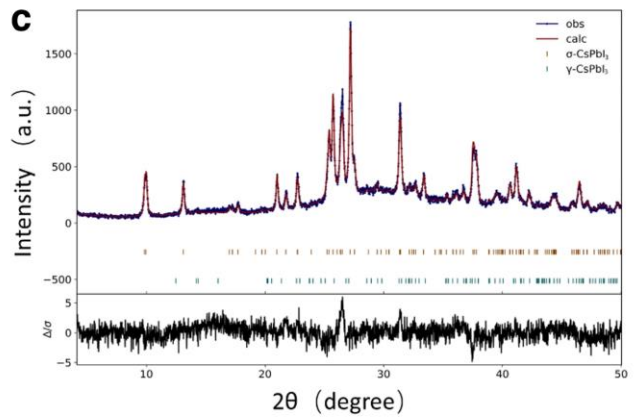


| Lattice parameters | Lattice parameters reported in ref. | Lattice parameters | Lattice parameters reported in ref. |
|---|---|---|---|
| a=10.4493 Å | a=10.4500(5) Å | a=8.6447 Å | a=8.6198(6) Å |
| b=4.7966 Å | b=4.7965(2) Å | b=8.8178 Å | b=8.8518(6) Å |
| c=17.7603 Å | c=17.7602(8) Å | c=12.5002 Å | c=12.5012(7) Å |
| α=90° | α=90° | α=90° | α=90° |
| β=90° | β=90° | β=90° | β=90° |
| γ=90° | γ=90° | γ=90° | γ=90° |
| V=890.172 Å$^3$ | V=890.20(7) Å$^3$ | V=952.857 Å$^3$ | V=953.852(11) Å$^3$ |
| Space group: *Pnma* | | Space group: *Pbnm* | |
| Crystal system: Orthorhombic (σ) | | Crystal system: orthorhombic (γ) | |
| Weight faction: 97.63% (sig: 0) | | Weight faction: 2.37% (sig: 0) | |
| $R_{wp}$=8.612% | | | |

**Supplementary Fig. 3. Examples of identifying the proportions of various $CsPbI_3$ phases within composites using XRD refinement. a** Rietveld refinement of powder XRD pattern of $(CsPbI_3)_{0.25}$ $(a_gZIF\text{-}62)_{0.75}$ composites sintering at 350 ℃, **b** $(CsPbI_3)_{0.5}(a_gZIF\text{-}62)_{0.5}$ composites prepared at 300 ℃ and **c** $(CsPbI_3)_{0.70}(a_gZIF\text{-}62)_{0.30}$ composites sintering at 275℃.

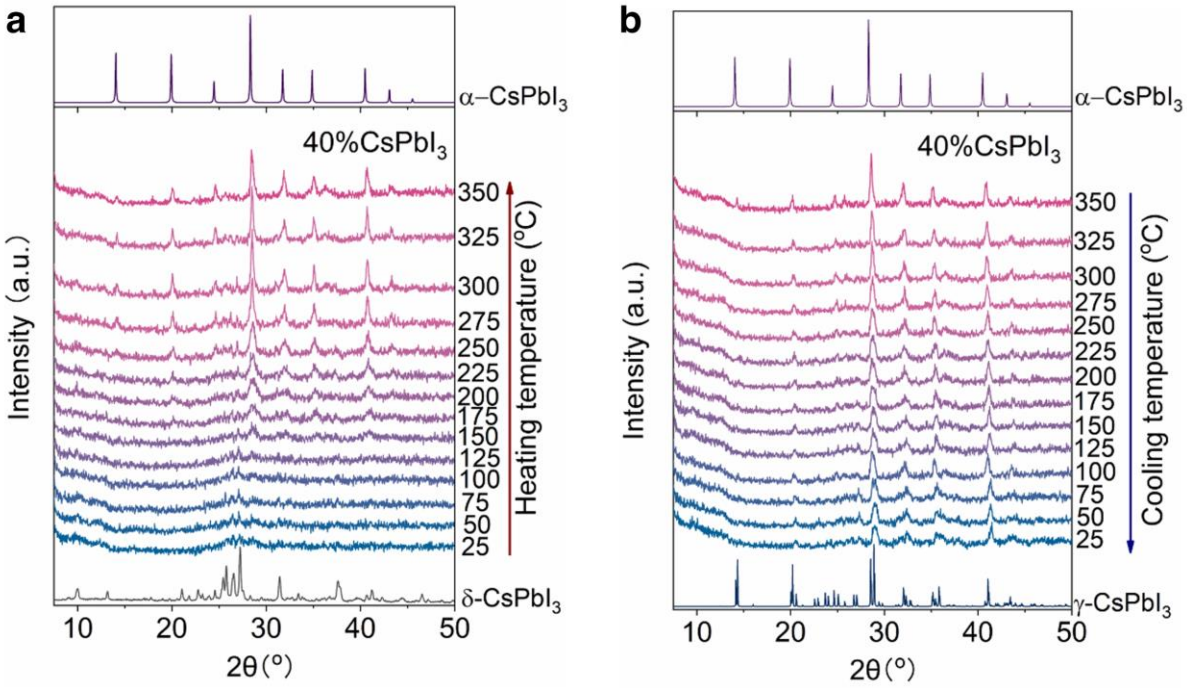


**Supplementary Fig. 4. a** *In-situ* XRD pattern of ($CsPbI_3$)($a_g$ZIF-62)(40/60) heated from 25 °C to 350 °C and **b** corresponding cooling down process. The temperature ramp is 20 °C/min under the protection of $N_2$. The reference XRD patterns of α-, γ- and δ-$CsPbI_3$ are retrieved from ref[1]. The intermediate β-phase was not resolved using our benchtop XRD instrument, due to resolution limits. During the cooling ramp, the perovskite gradually lowered its symmetry, resulting in the formation of the orthorhombic γ-phase upon returning to room temperature.

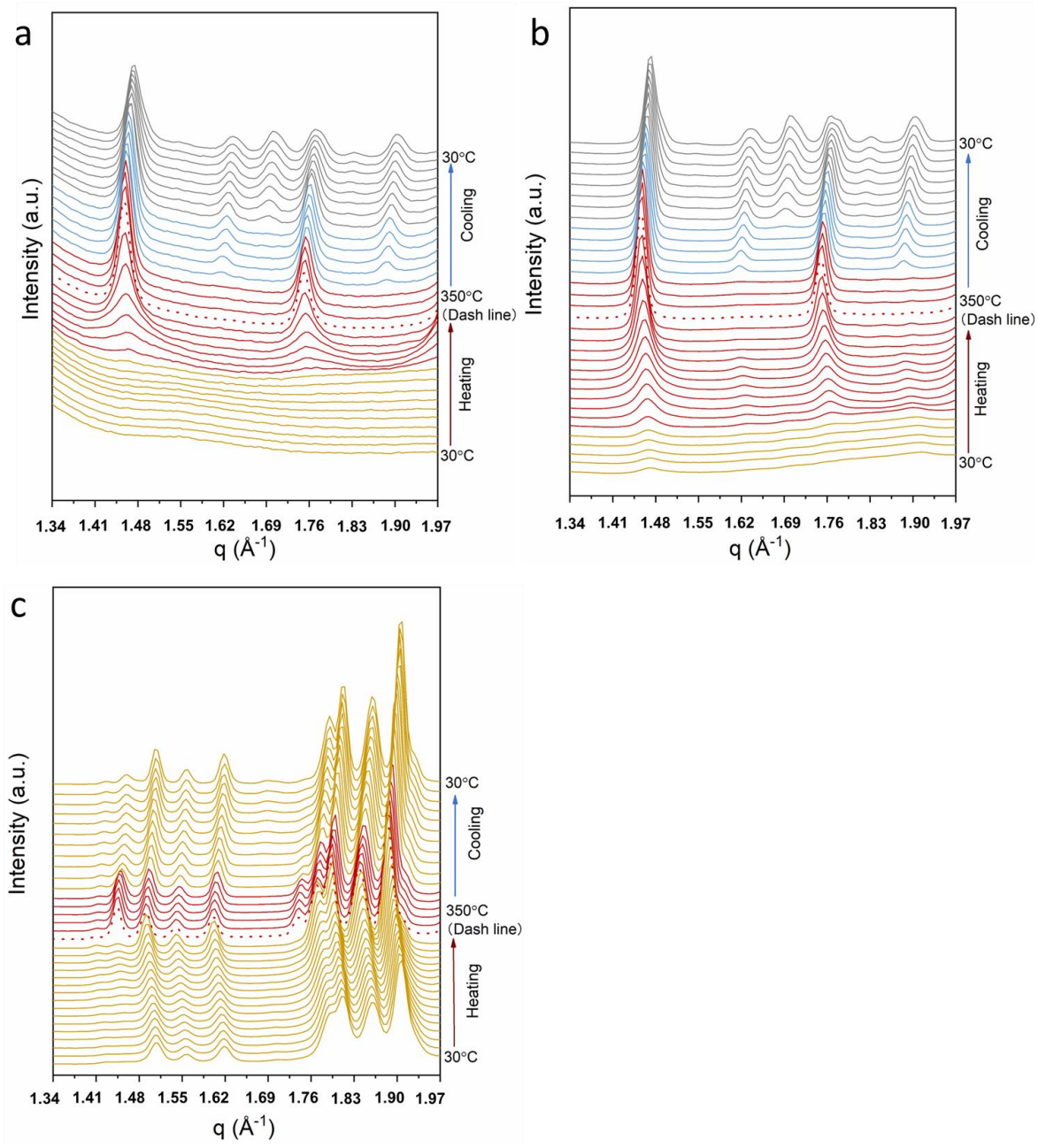


**Supplementary Fig. 5. High resolution *in situ* synchrotron powder XRD for different samples during sintering and quenching. The dominating $CsPbI_3$ phases are color-coded as: δ (yellow), α (red), β (blue) and γ (grey). a** ($CsPbI_3$)( $a_g$ZIF-62)(5/95), **b** ($CsPbI_3$)($a_g$ZIF-62)(40/60) and **c** ($CsPbI_3$)( $a_g$ZIF-62)(55/45).

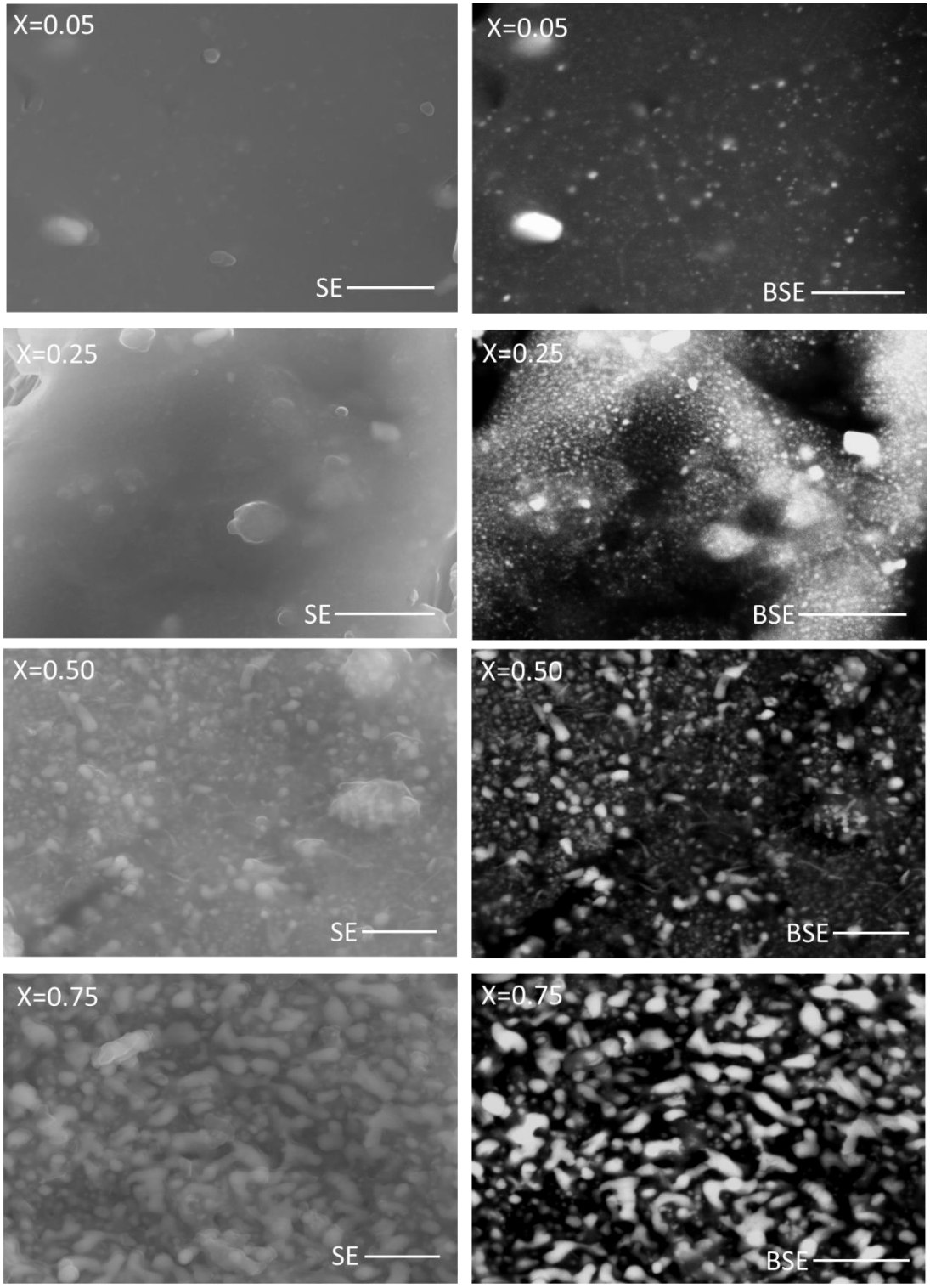


**Supplementary Fig. 6. SEM secondary electron image (SE, left) and backscattering image (BSE, right) of $(CsPbI_3)_X(a_gZIF\text{-}62)_Y$ composites sintered at 350 °C.** The scale bar is 1μm.

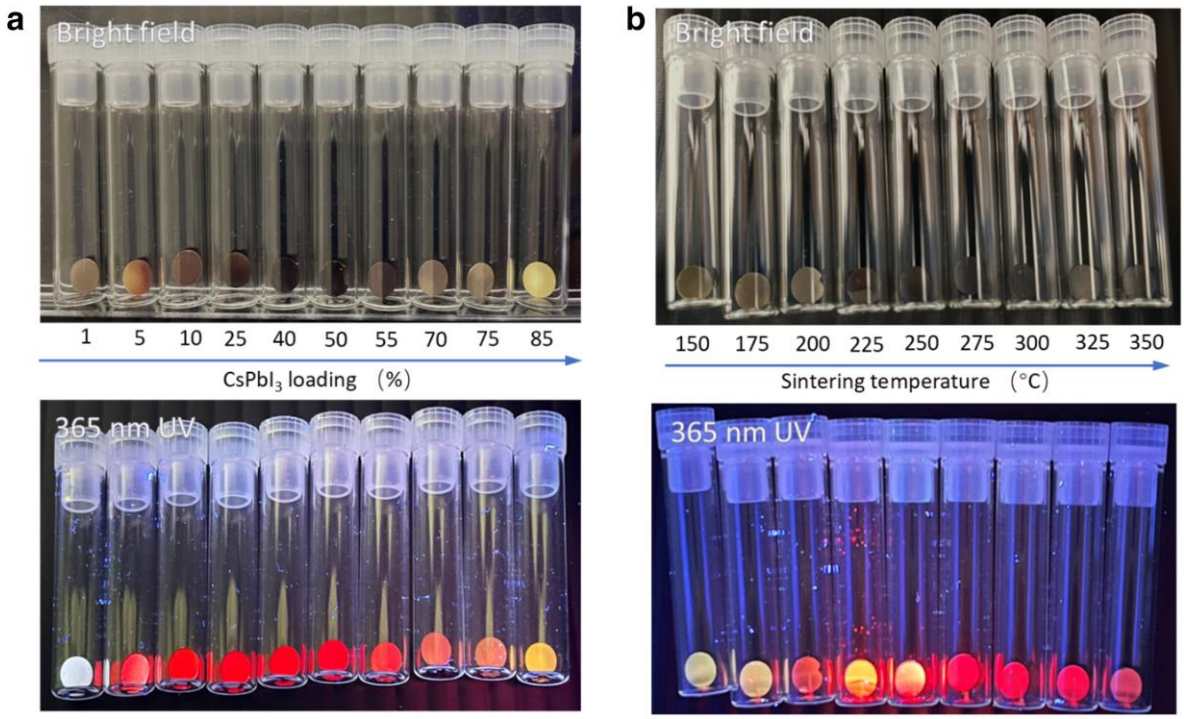


**Supplementary Fig. 7. PL emission of the composites. a** Optical images of the $(CsPbI_3)_X(a_gZIF\text{-}62)_Y$ composites sintering at 275 ℃ with different $CsPbI_3$ components and **b** $(CsPbI_3)_{0.25}(a_gZIF\text{-}62)_{0.75}$ composites with various sintering temperatures.

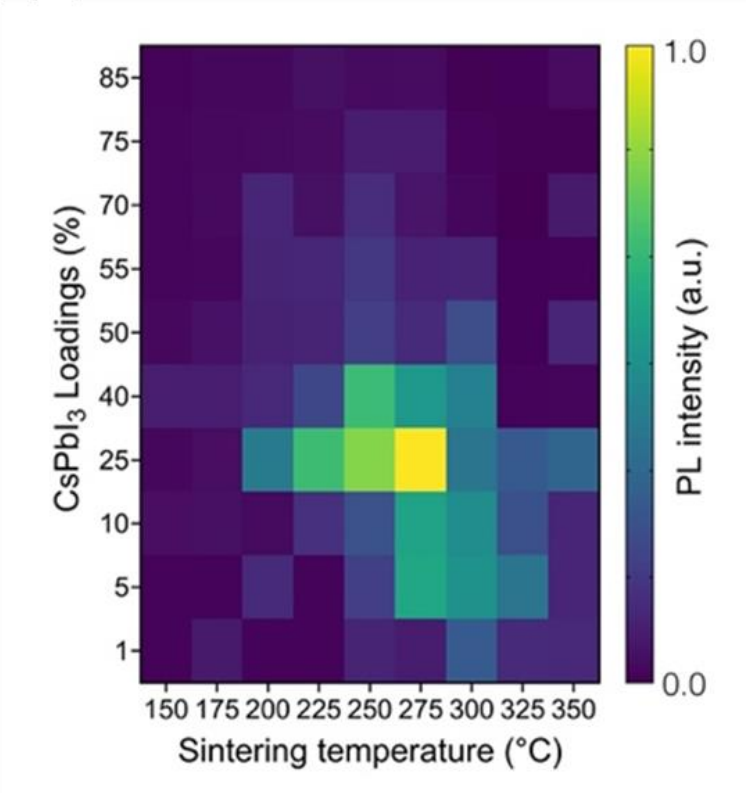


**Supplementary Fig. 8. Relative PL intensity of different $(CsPbI_3)_X(a_gZIF\text{-}62)_Y$ composites.**

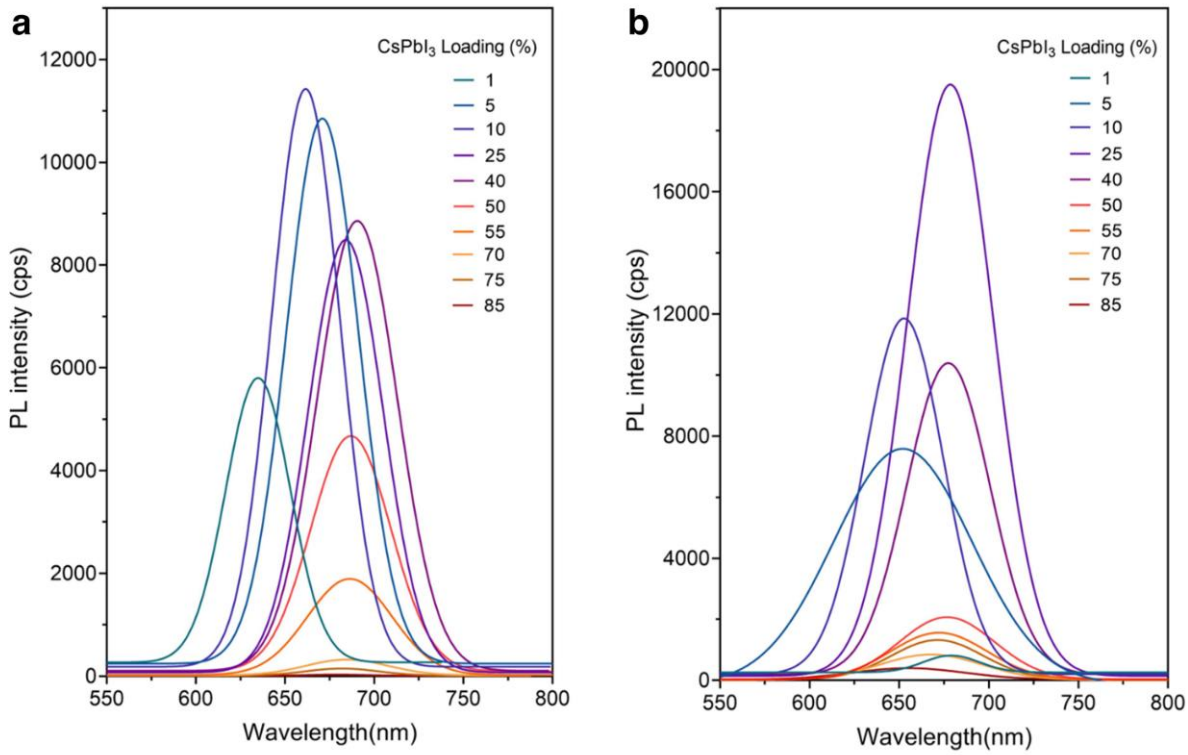


**Supplementary Fig. 9. PL profiles of different $CsPbI_3$ loading samples sintered at a 300℃ and b 275℃.**

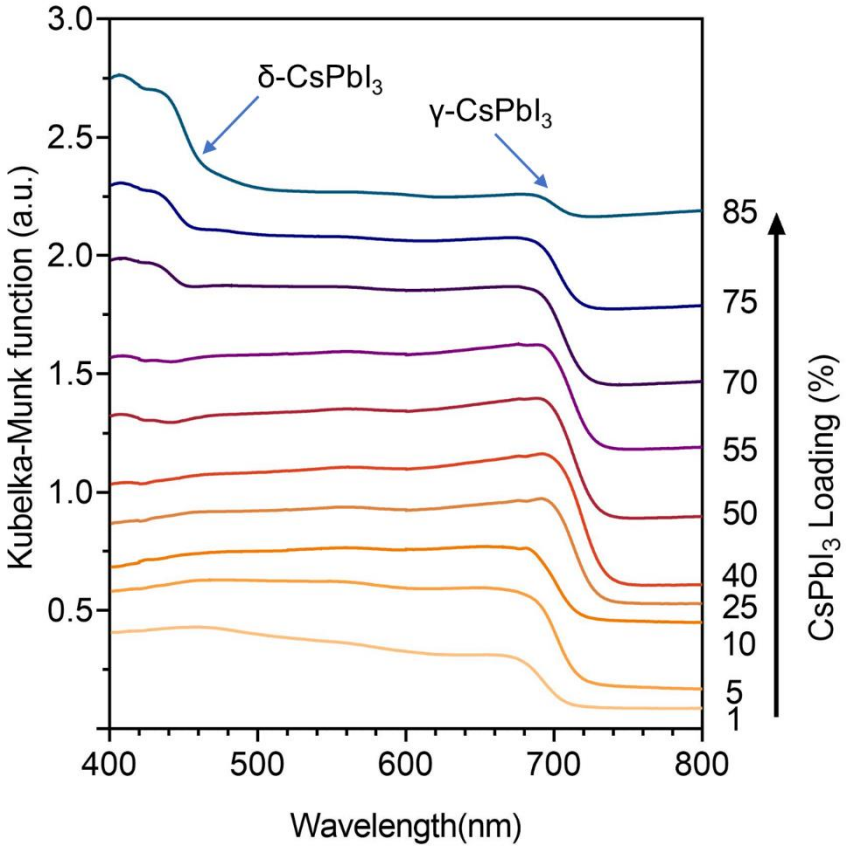


**Supplementary Fig. 10. UV-Vis absorption spectra for different $CsPbI_3$ percentages composites sintered at 300 ℃.**

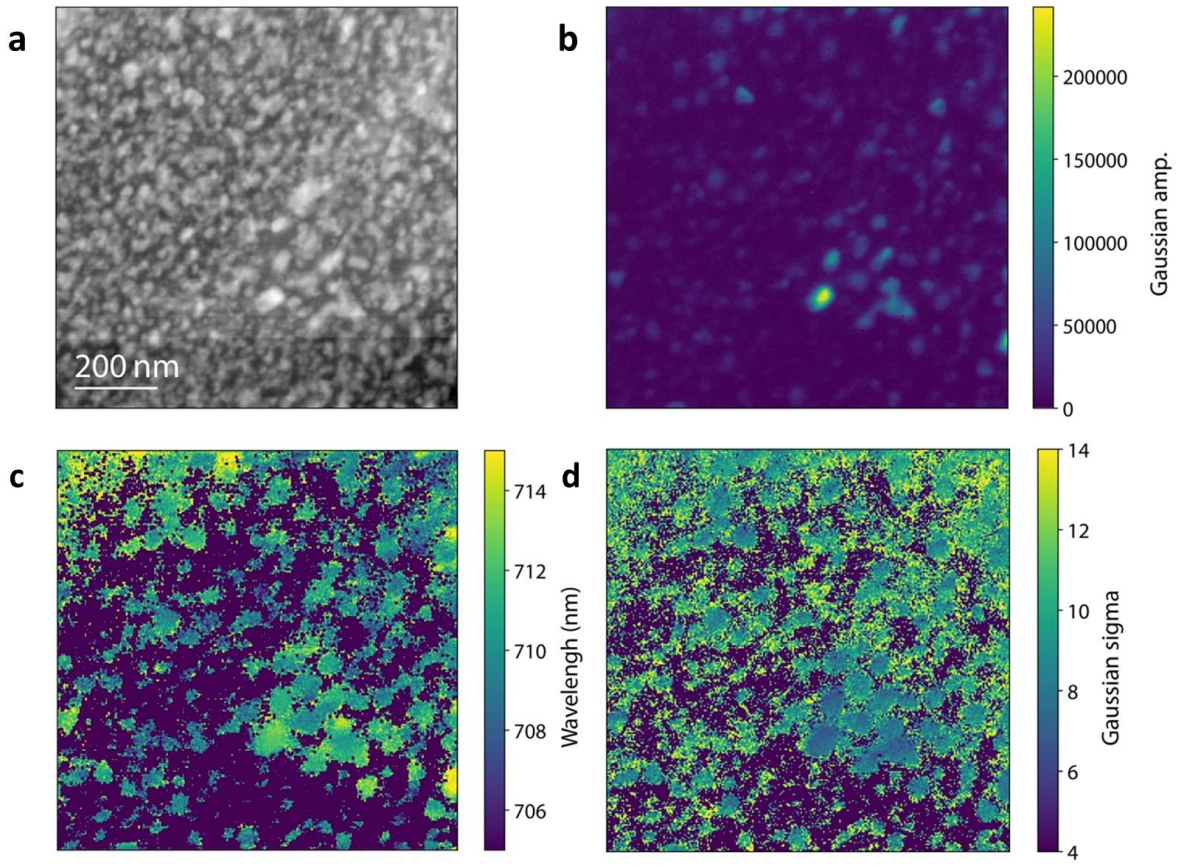


**Supplementary Fig. 11. Cathodoluminescence (CL)-STEM characterisation of the $(CsPbI_3)_{0.40}(a_gZIF\text{-}62)_{0.60}$ composites sintered at 350 °C and thinned with FIB-SEM. a** ADF-STEM image. **b** Mapping of the Gaussian fitted CL peak intensity. **c** Mapping of the Gaussian fitted CL peak position values and **d** Gaussian fitted σ (nm) values.

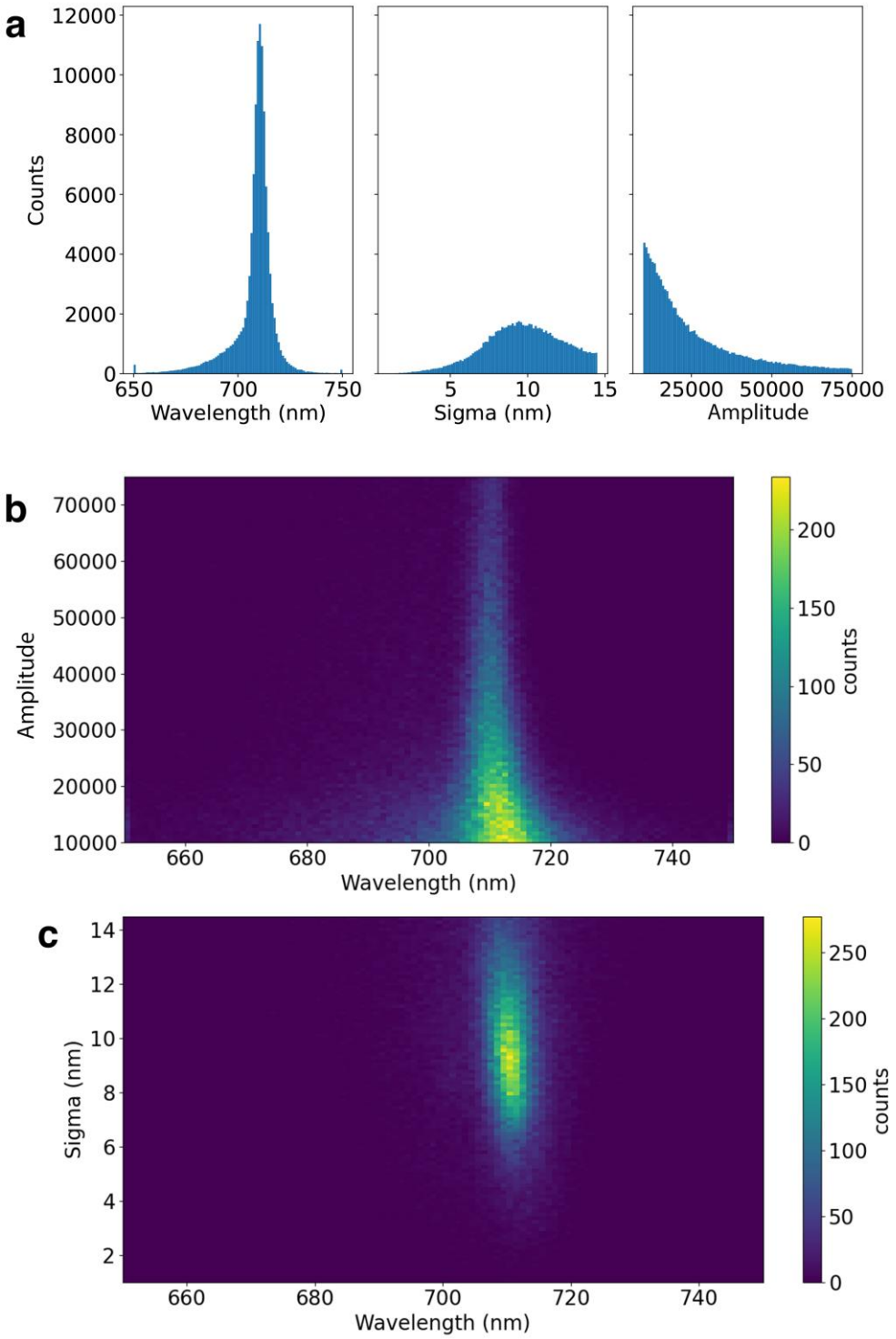


**Supplementary Fig. 12. CL-STEM characterisation of the $(CsPbI_3)_{0.1}(a_gZIF\text{-}62)_{0.9}$ composites sintered at 350 °C.** CL data cubes have been acquired from a total project area of 6.9 µm$^2$. A one Gaussian model was fitted to each spectrum. **a** Histograms of the fitted coefficients across the whole measured area: Gaussian peak center, sigma and amplitude. **b, c** 2D histogram of the amplitude versus wavelength and sigma versus wavelength shows that correlations exist. Lower wavelength peaks are associated to higher intensities.

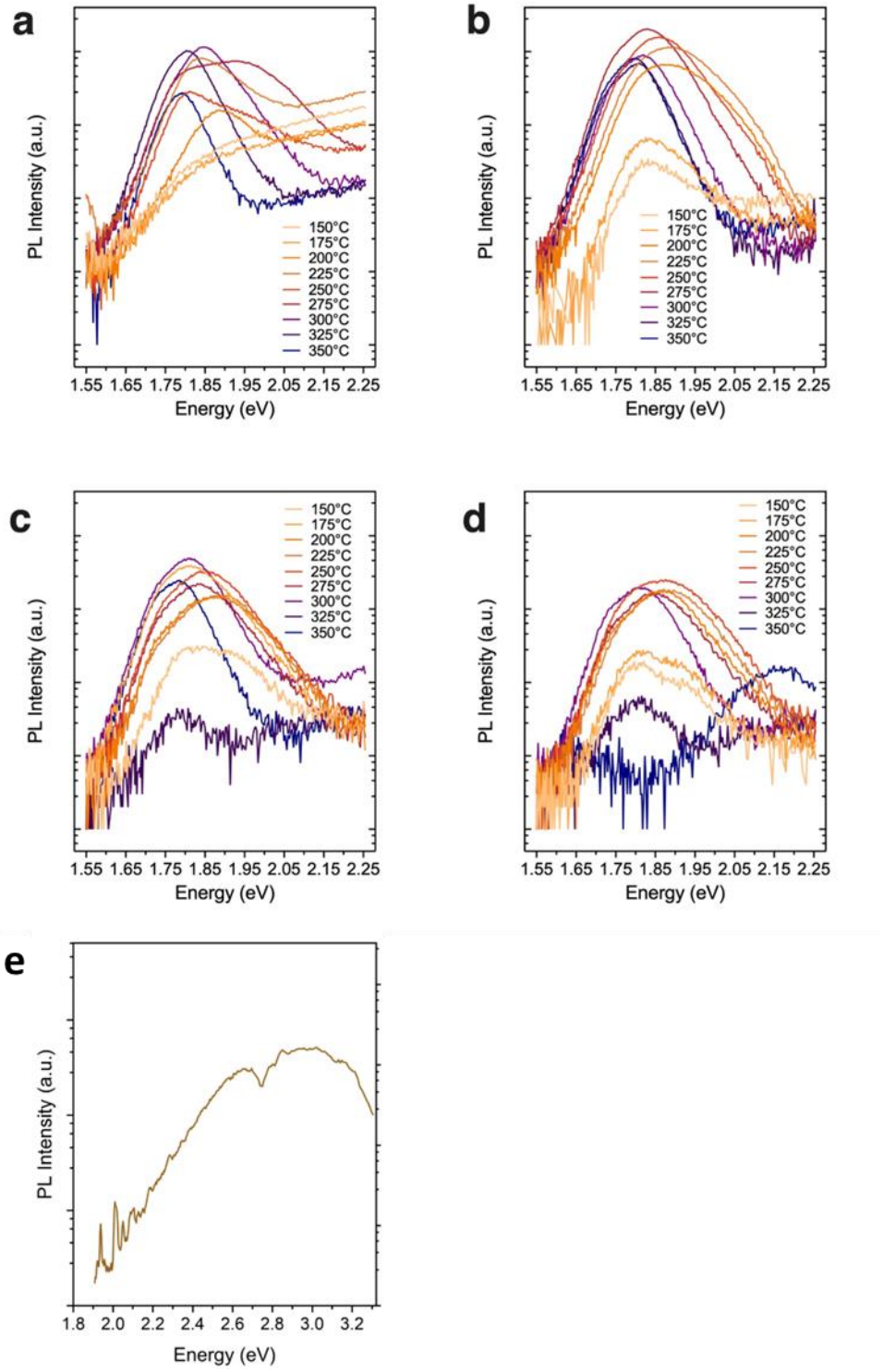


**Supplementary Fig. 13. PL spectra shown in log scale for a $(CsPbI_3)_{0.05}(a_gZIF\text{-}62)_{0.95}$ composite, b $(CsPbI_3)_{0.25}(a_gZIF\text{-}62)_{0.75}$ composite, c $(CsPbI_3)_{0.50}(a_gZIF\text{-}62)_{0.50}$ composite, d $(CsPbI_3)_{0.55}(a_gZIF\text{-}62)_{0.45}$ composite and (e) pure $a_g$ZIF-62.**

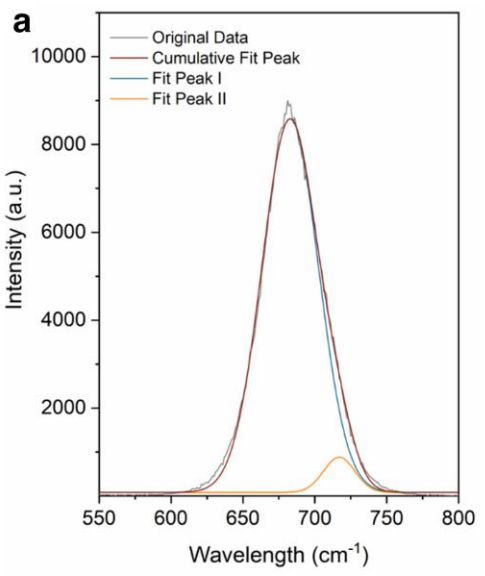


**b**

| Model | Gauss | |
|---|---|---|
| Equation | $y=y_0+(A/(w*sqrt(pi/2)))*exp(-2*((x-x_c)/w)^2)$ | |
| Plot | Peak I | Peak II |
| $y_0$ | 81.13 ± 9.77 | 81.13 ± 9.77 |
| $x_c$ | 682.82 ± 0.20 | 716.94 ± 0.97 |
| w | 39.27 ± 0.33 | 21.78 ± 1.75 |
| A | 418305.79 ± 3918.98 | 21896.09 ± 3476.46 |
| Reduced Chi-Sqr | 13025.42 | |
| R-Square (COD) | 0.998 | |
| Adj. R-Square | 0.998 | |

**Supplementary Fig. 14. Representative PL fitting with two-Gaussian function. a** PL curve of $(CsPbI_3)_{0.25}(a_gZIF\text{-}62)_{0.75}$ composite sintering at 300 ℃ fitted by two peaks Gaussian fits, the peaks were noted as Peak I and Peak II. **b** The summary of fitting results and peak parameters. Peak I represents the high energy peak and the Peak II represents the low energy peak.

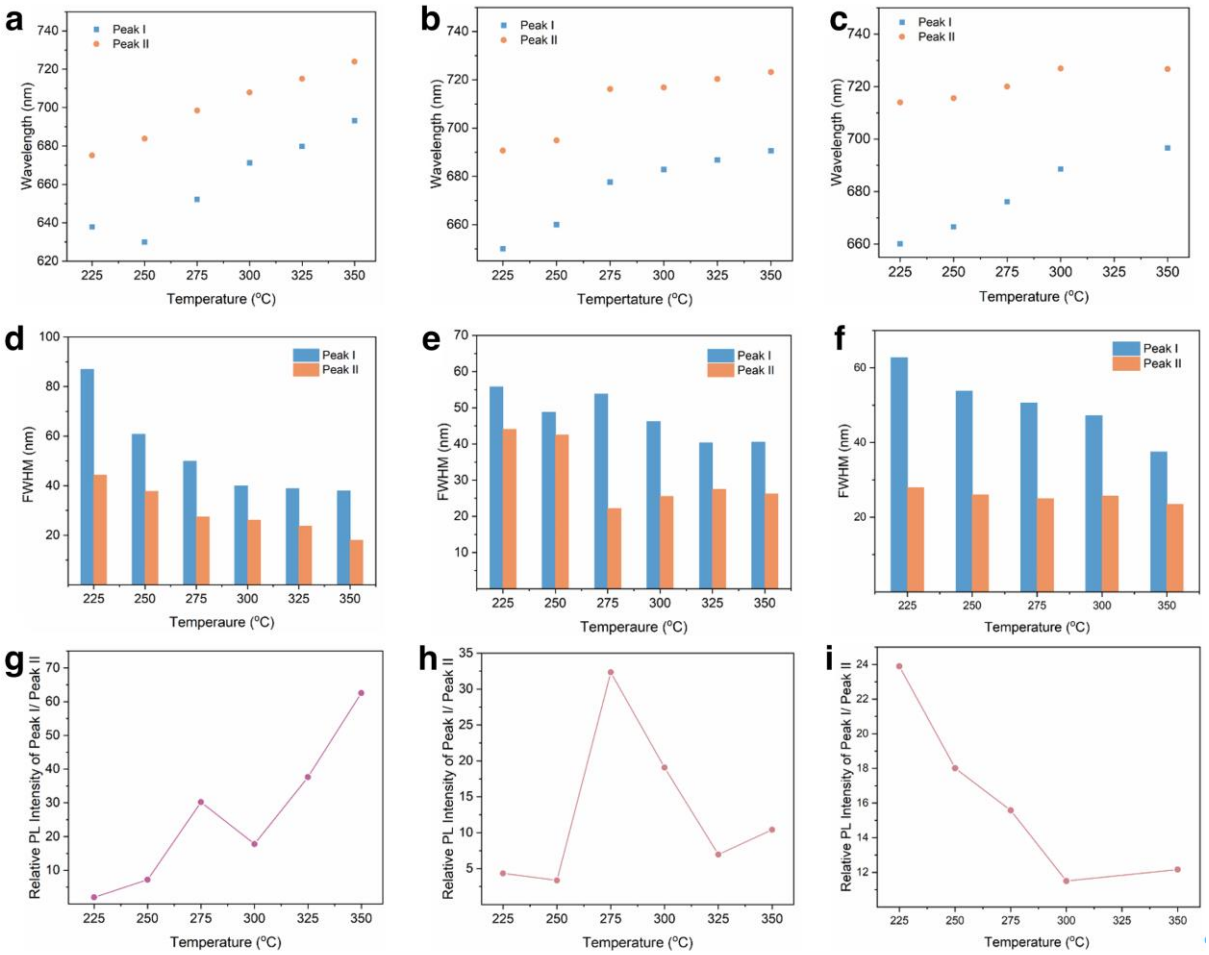


**Supplementary Fig. 15. Summary of the two-Gaussian fitting of PL, where Peak I represents the high energy peak and the Peak II represents the low energy peak.** The extracted peak positions for **a** $(CsPbI_3)_{0.1}(a_gZIF\text{-}62)_{0.9}$, **b** $(CsPbI_3)_{0.25}(a_gZIF\text{-}62)_{0.75}$ and **c** $(CsPbI_3)_{0.40}(a_gZIF\text{-}62)_{0.60}$ composites. The summary of peak bandwidths from **d** $(CsPbI_3)_{0.1}(a_gZIF\text{-}62)_{0.9}$, **e** $(CsPbI_3)_{0.25}(a_gZIF\text{-}62)_{0.75}$ and **f** $(CsPbI_3)_{0.40}(a_gZIF\text{-}62)_{0.60}$ composites. The relative intensity of Peak I and Peak II from **g** $(CsPbI_3)_{0.1}(a_gZIF\text{-}62)_{0.9}$, **h** $(CsPbI_3)_{0.25}(a_gZIF\text{-}62)_{0.75}$ and **i** $(CsPbI_3)_{0.40}(a_gZIF\text{-}62)_{0.60}$ composites.

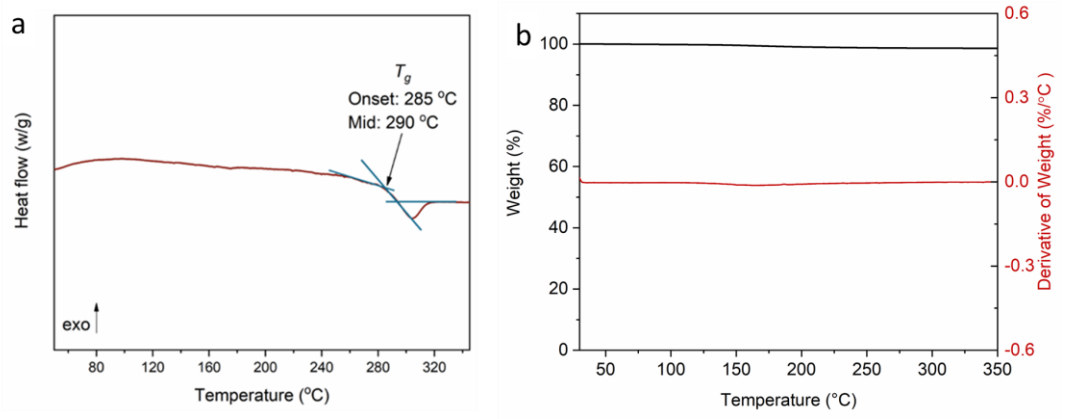


**Supplementary Fig. 16. DSC and TGA results upon sintering to 350 ℃. Data was collected under constant flowing nitrogen (20 mL/min). a** DSC results for melt-quenched $a_g$ZIF-62 and **b** TGA results for ($CsPbI_3$)( $a_g$ZIF-62)(40/60)**.** The temperature ramp rate was 20 °C /min.

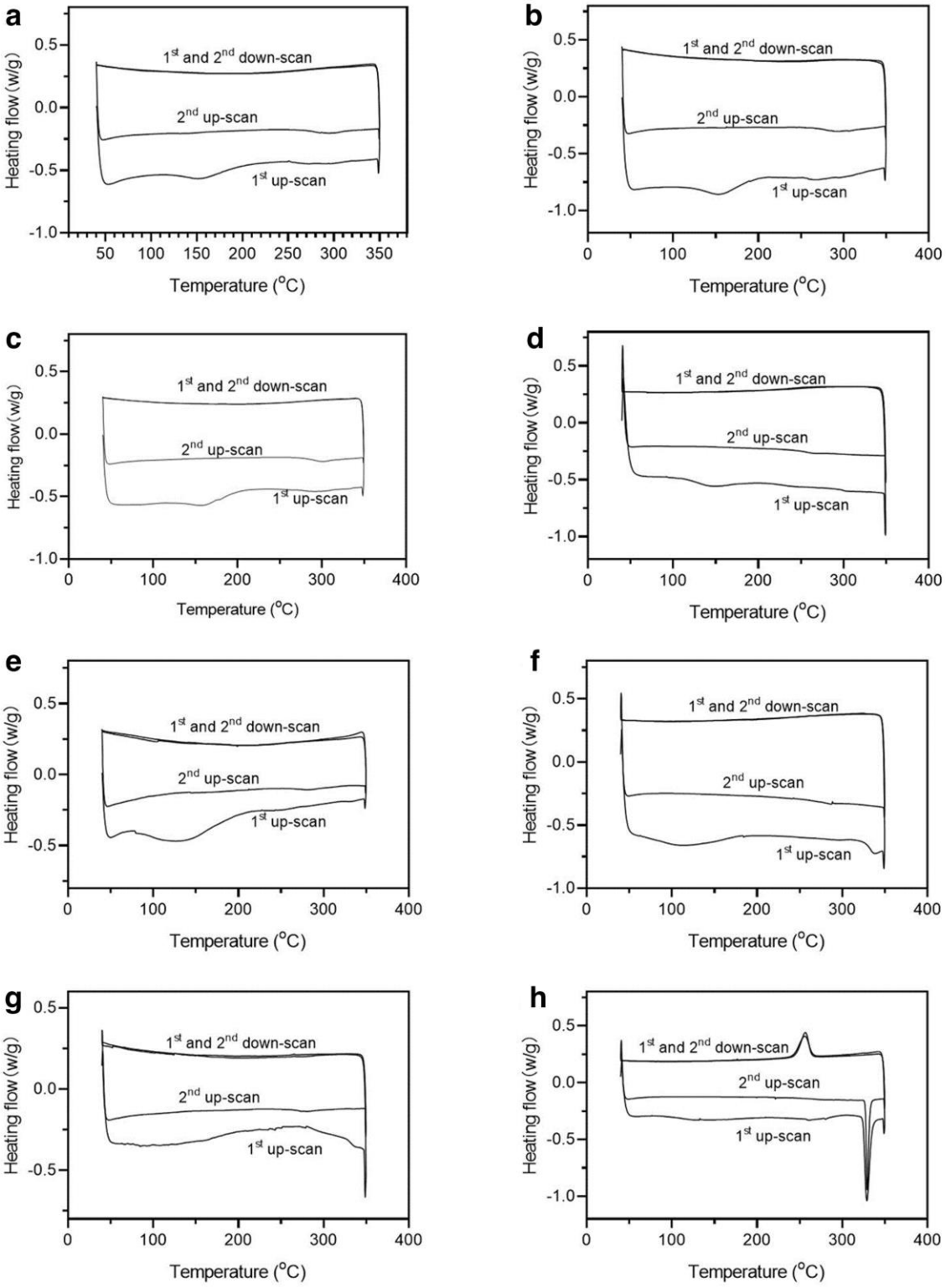


**Supplementary Fig. 17. DSC data of $(CsPbI_3)_x(a_gZIF\text{-}62)_Y$ composites with different $CsPbI_3$ loadings. a** $CsPbI_3)_{0.01}(a_gZIF\text{-}62)_{0.99}$, **b** $(CsPbI_3)_{0.05}(a_gZIF\text{-}62)_{0.95}$, **c** $(CsPbI_3)_{0.10}(a_gZIF\text{-}62)_{0.90}$, **d** $(CsPbI_3)_{0.25}(a_gZIF\text{-}62)_{0.75}$, **e** $CsPbI_3)_{0.40}(a_gZIF\text{-}62)_{0.60}$, **f** $CsPbI_3)_{0.50}(a_gZIF\text{-}62)_{0.50}$, **g** $CsPbI_3)_{0.55}(a_gZIF\text{-}62)_{0.45}$ and **h** $CsPbI_3)_{0.75}(a_gZIF\text{-}62)_{0.25}$ composites. The temperature ramping rate for the first up-scan was 20 °C/min, and the ramping rate was 10 °C/min during the DSC cooling and second up-scan.

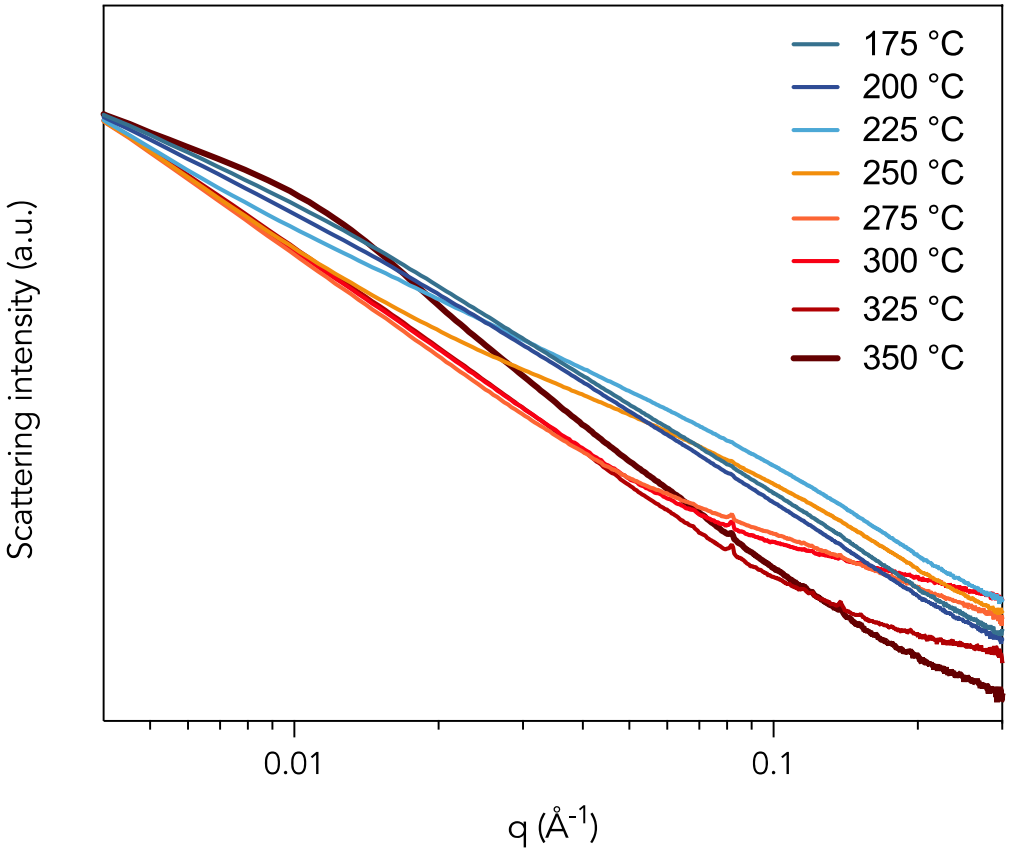


**Supplementary Fig. 18.** ***Ex-situ*** **synchrotron small angel scattering (SAXS) of $(CsPbI_3)_{0.1}(agZIF\text{-}62)_{0.9}$ fabricated with different sintering temperatures.** The spike at *ca*. 0.08 $Å^{-1}$ is attributed to the detector configuration.

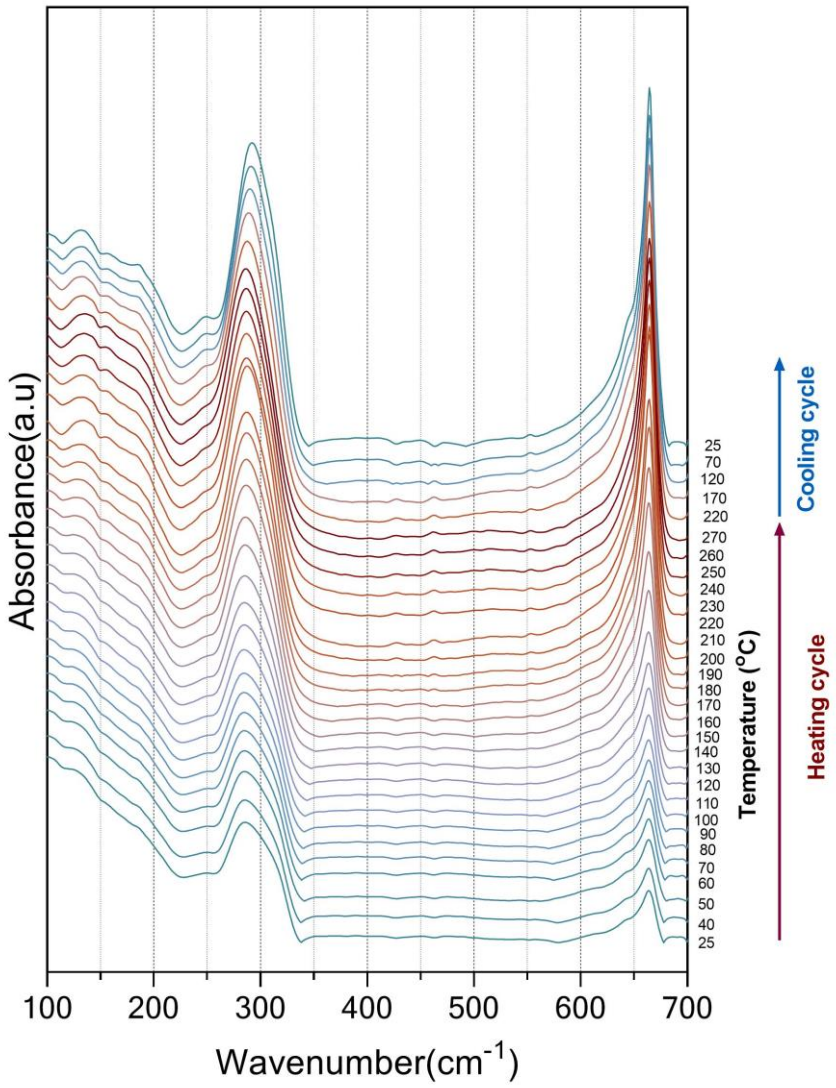


**Supplementary Fig. 19.** Temperature-resolved *in-situ* THz FarIR spectra for $(CsPbI_3)(a_gZIF\text{-}62)(10/90)$ composites during heating and cooling ramps. Ramp rate was 10°C/min.

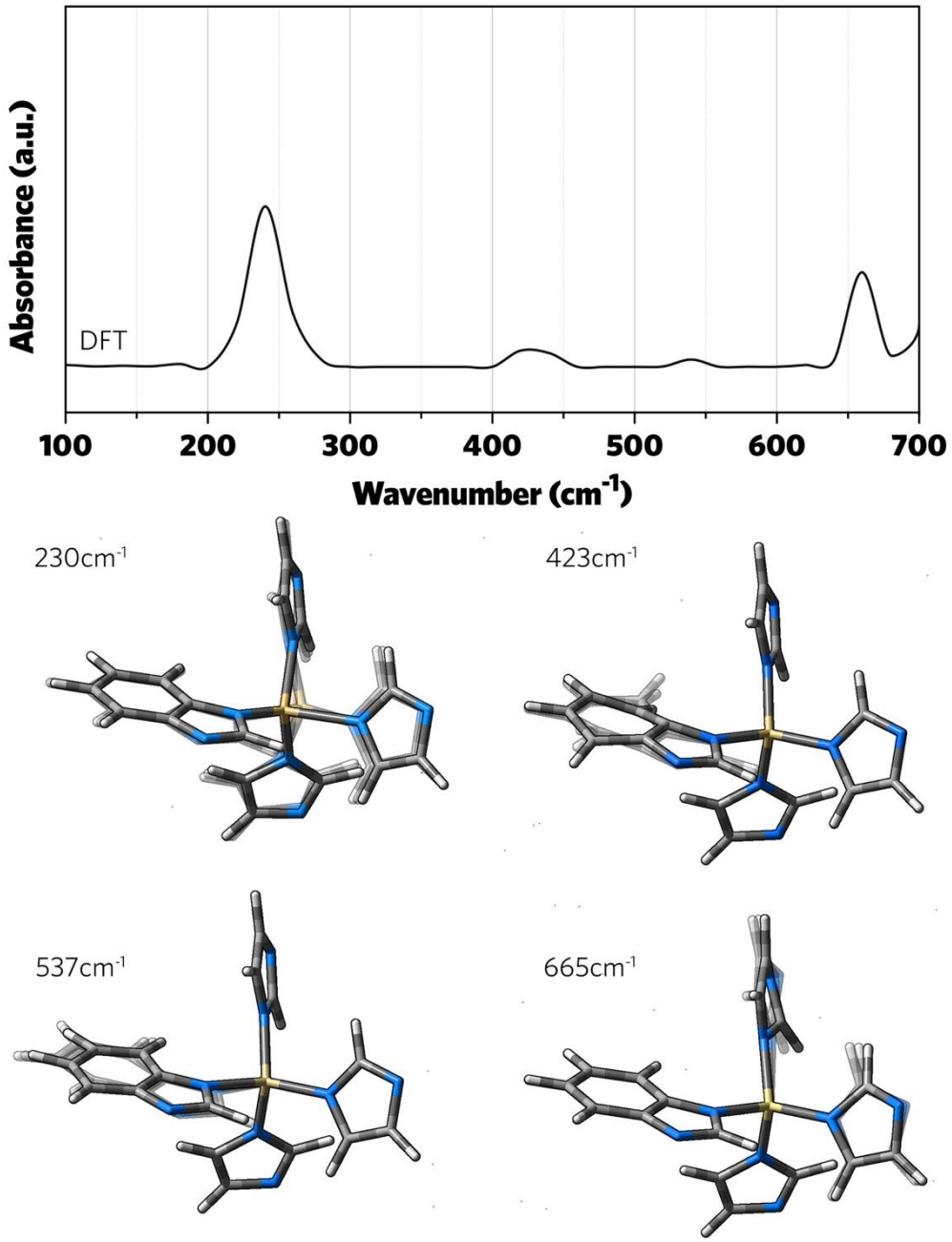


**Supplementary Fig. 20.** DFT calculations of the ZIF-62 THz absorbance spectrum. The scheme represents the vibration and deformation movement of the corresponding features. More detailed DFT calculation procedures can be found in our previous publication[2].

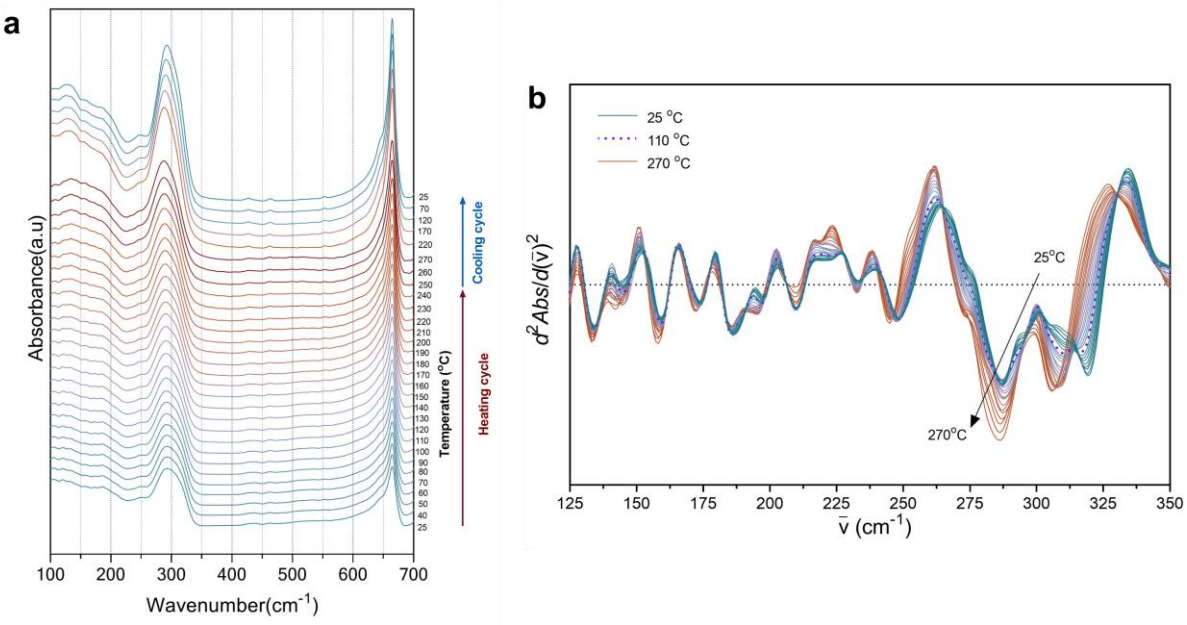


**Supplementary Fig. 21. a Temperature-resolved *in-situ* THz FarIR spectra for ($CsPbI_3$)($a_g$ZIF-62)(1/99) composites and b corresponding second derivative spectra.** The sample were heated to 270 ℃ and cooling back to room temperature under Ar protections.

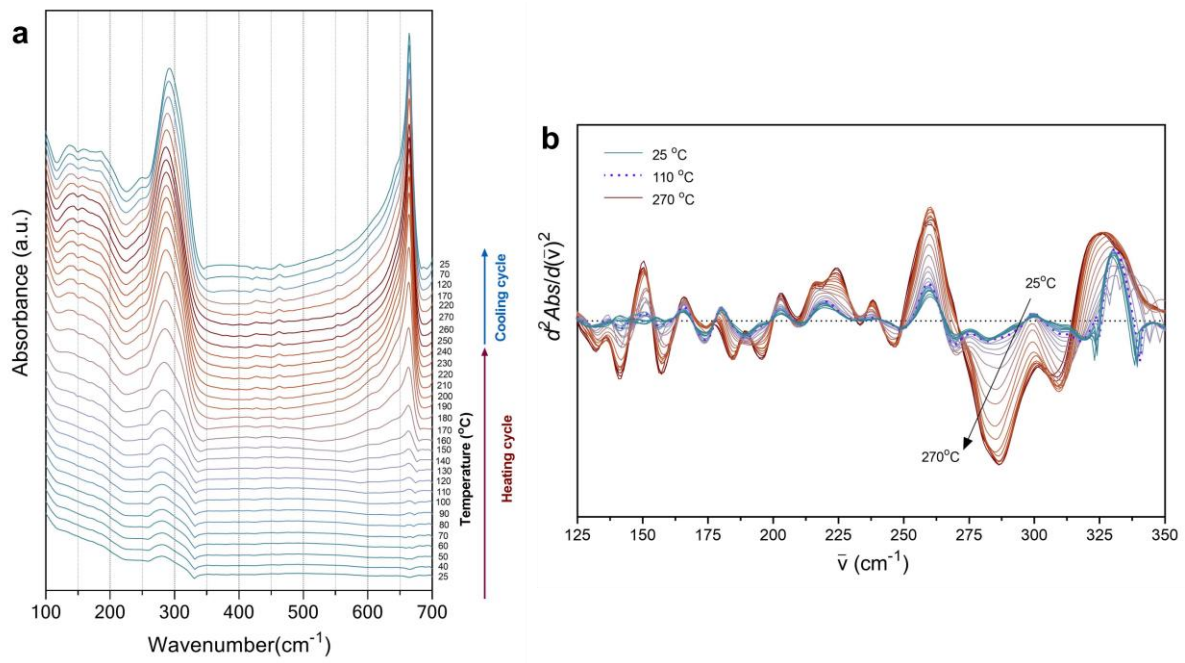


**Supplementary Fig. 22. a Temperature-resolved *in-situ* THz FarIR spectra for ($CsPbI_3$)($a_g$ZIF-62)(25/75) composites and b corresponding second derivative spectra.** The sample were heated to 270 ℃ and cooling back to room temperature under Ar protections.

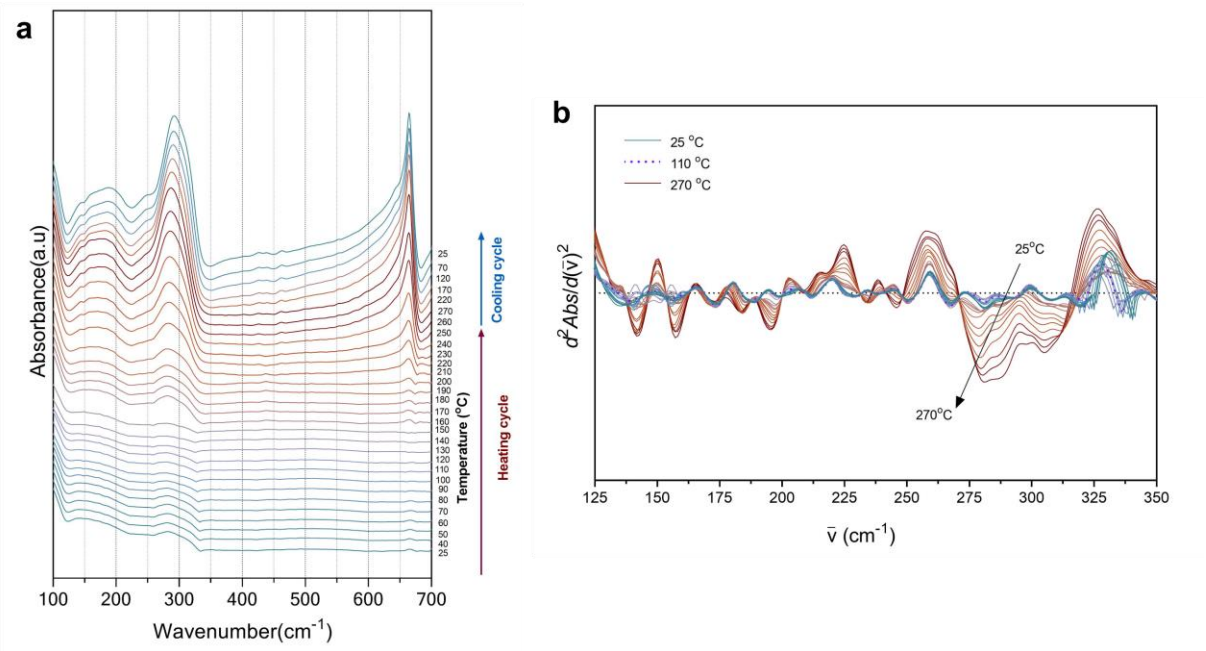


**Supplementary Fig. 23. a Temperature-resolved *in-situ* THz FarIR spectra for ($CsPbI_3$)($a_g$ZIF-62)(55/45) composites and b corresponding second derivative spectra.** The sample were heated to 270 ℃ and cooling back to room temperature under Ar protections.

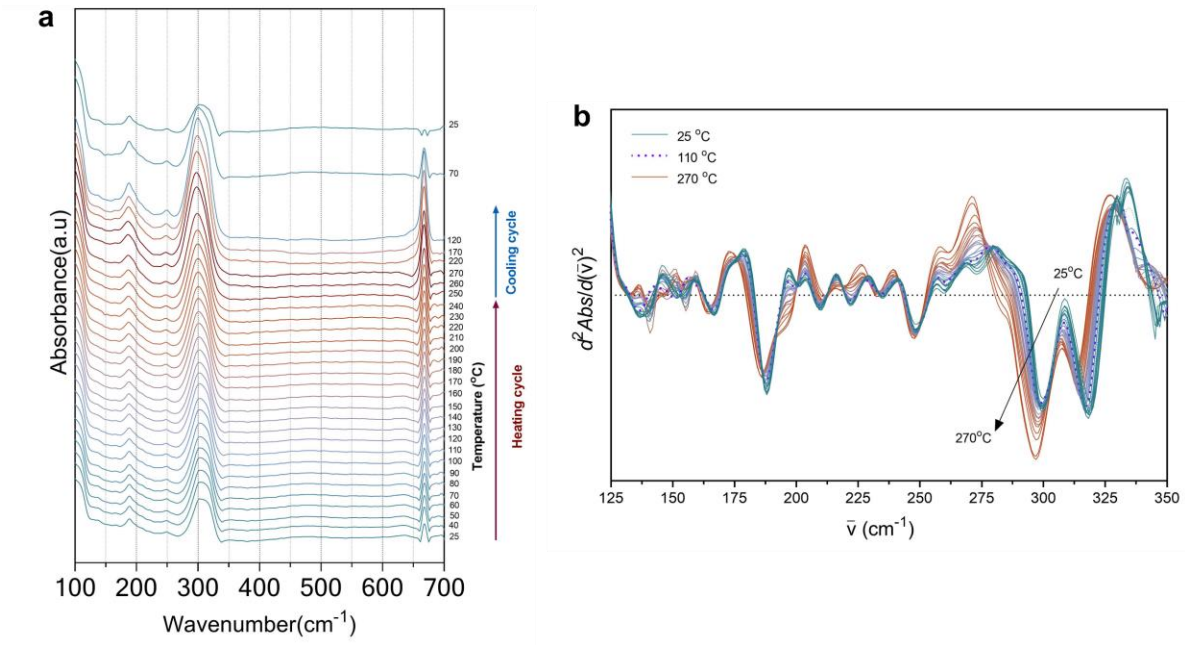


**Supplementary Fig. 24. a Temperature-resolved *in-situ* THz FarIR spectra for ($CsPbI_3$)($a_g$ZIF-62)(85/15) composites and b corresponding second derivative spectra.** The sample were heated to 270 ℃ and cooling back to room temperature under Ar protections.

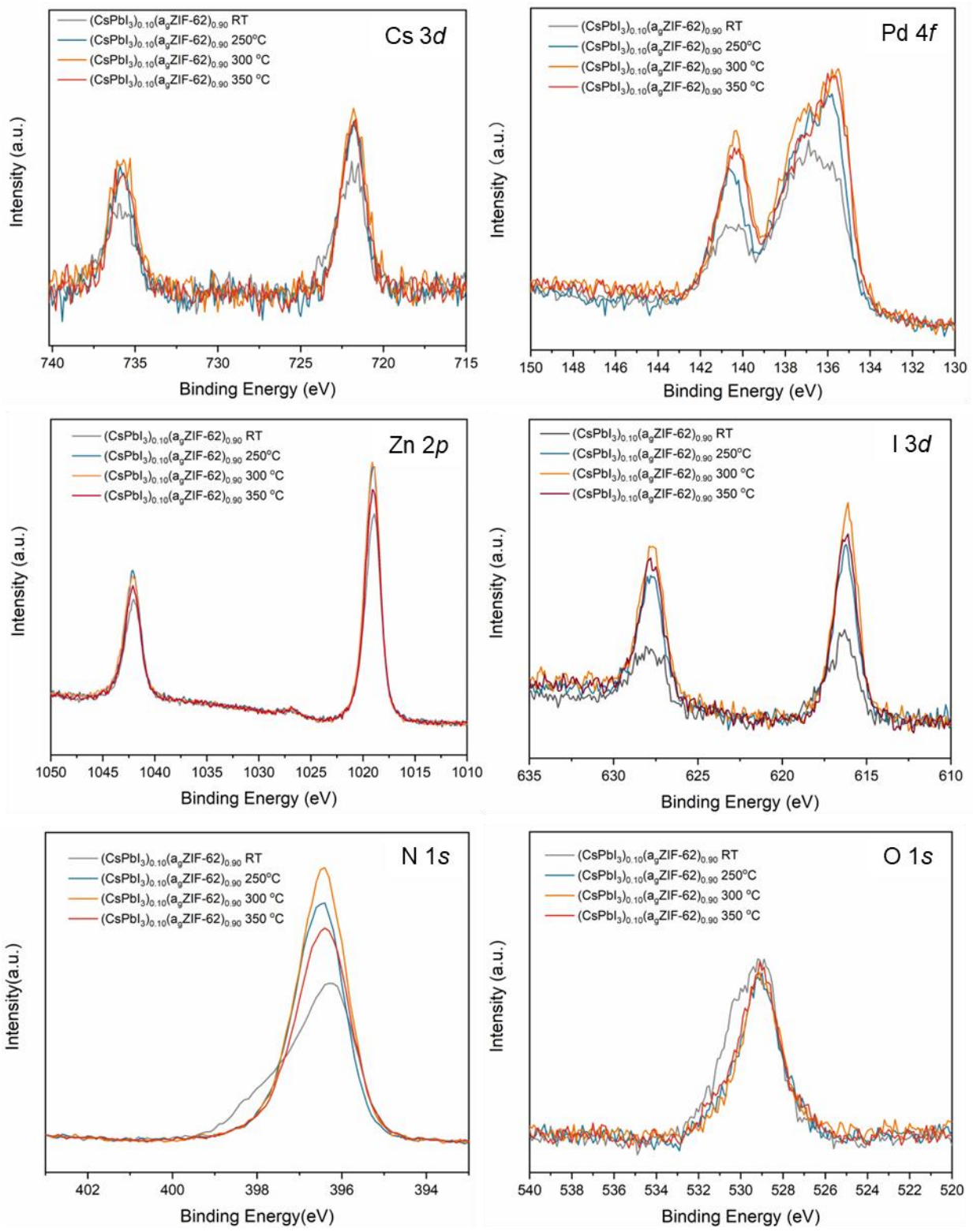


**Supplementary Fig. 25. X-ray photoelectron spectroscopy (XPS) of $(CsPbI_3)_{0.1}(a_gZIF\text{-}62)_{0.9}$ composites at different sintering temperatures.**

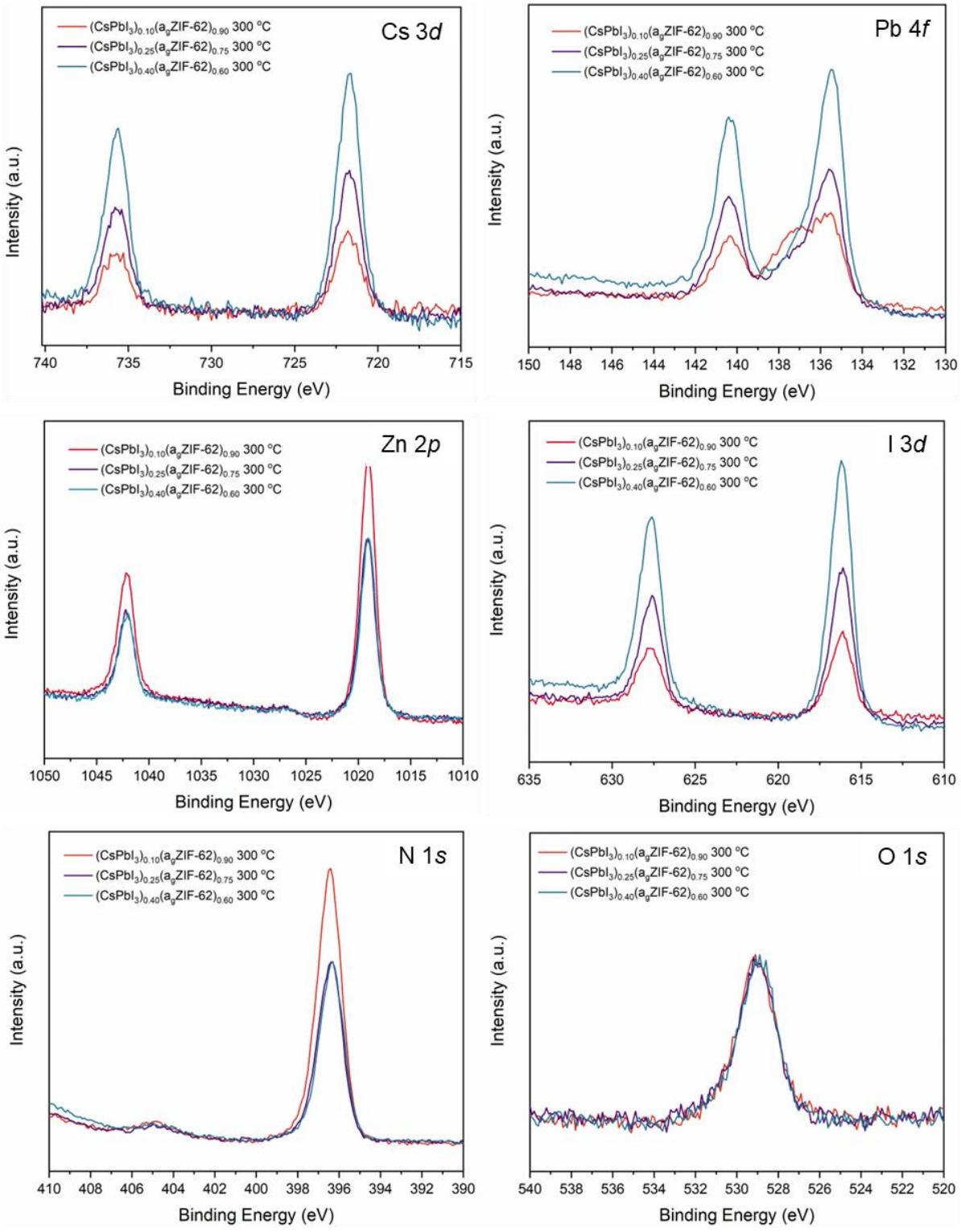


**Supplementary Fig. 26. X-ray photoelectron spectroscopy (XPS) of $(CsPbI_3)_x(a_gZIF\text{-}62)_Y$ composites sintering at 300 ℃ with different components.**

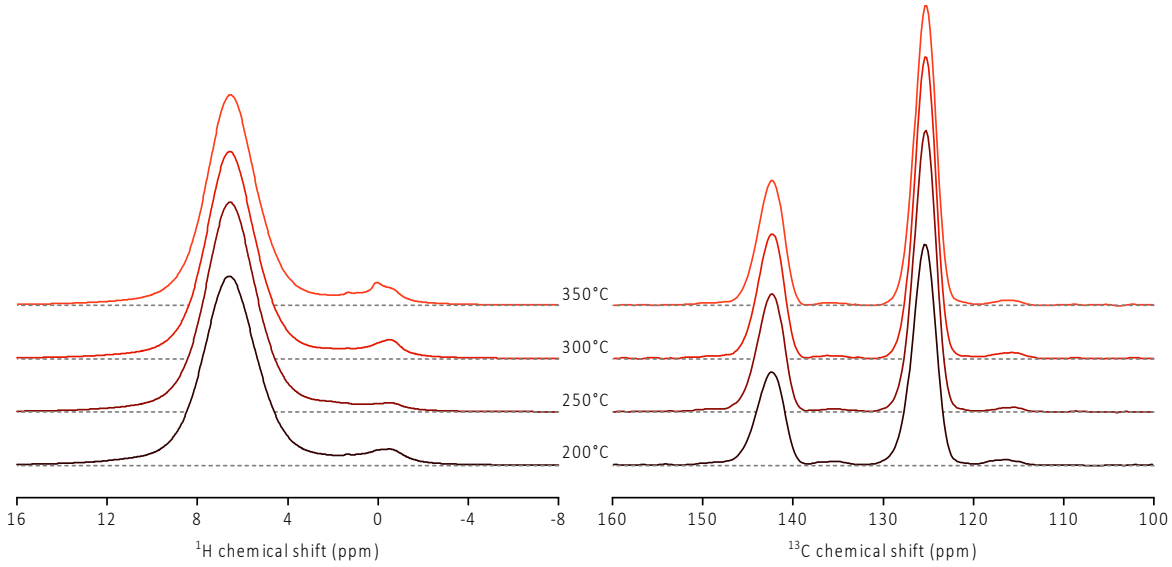


**Supplementary Fig. 27. $^{1}$H and $^{13}$C MAS NMR spectra of $(CsPbI_3)_{0.25}(a_gZIF\text{-}62)_{0.75}$ composites sintered at 200, 250, 300, and 350 °C.**

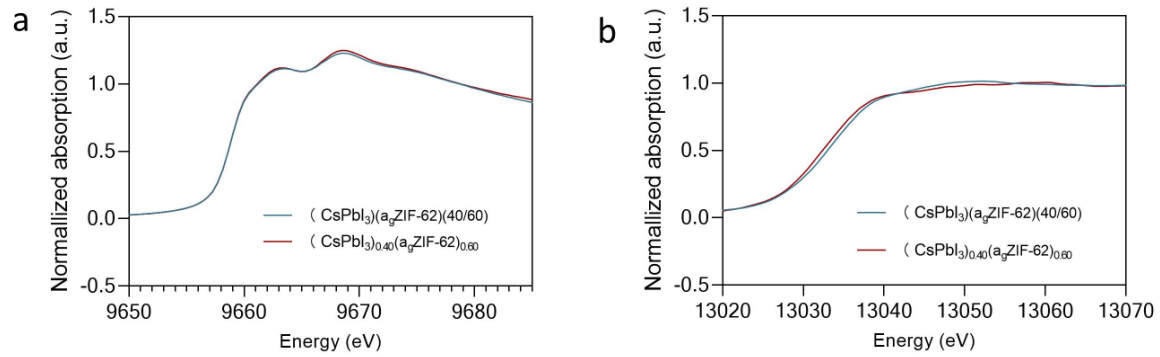


**Supplementary Fig. 28. X-ray absorption of 40 wt% $CsPbI_3$ / $a_g$ZIF-62 composites prior and after 350 °C sintering. a** Zn K edge X-ray absorption spectrum near edge structure (XANES) and **b** Pb $L_3$-edge XANES.

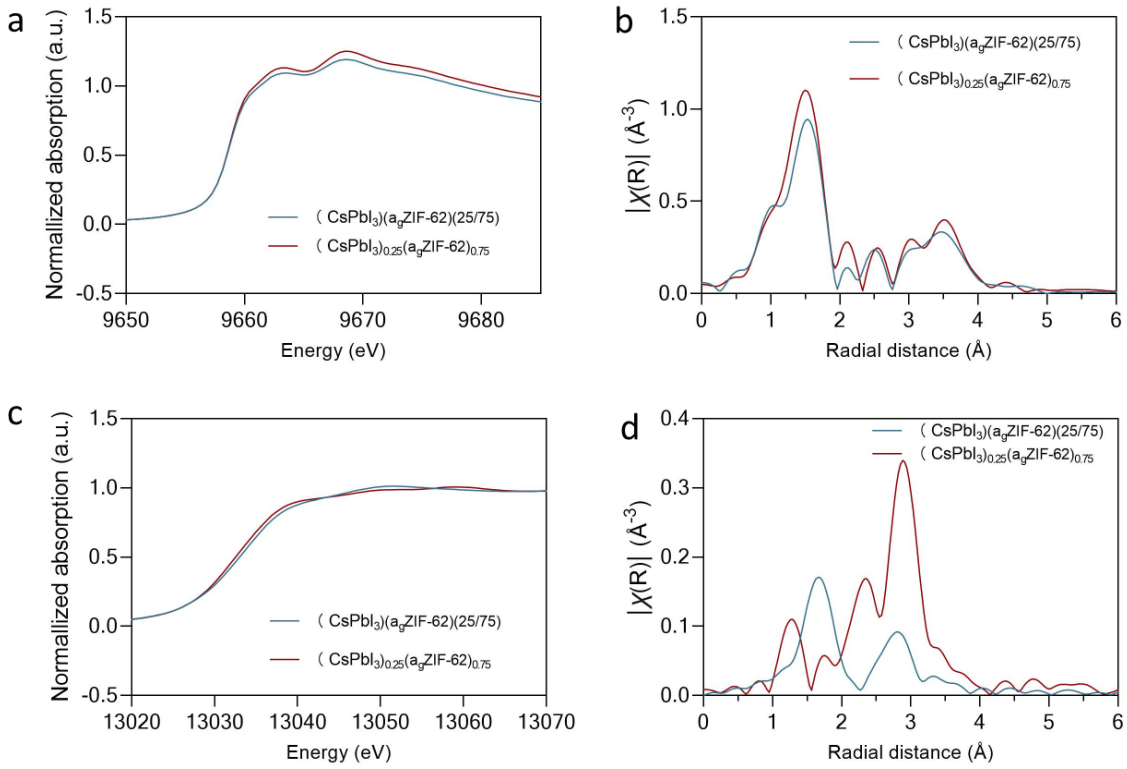


**Supplementary Fig. 29. X-ray absorption of 25 wt% $CsPbI_3$ / $a_g$ZIF-62 composites prior and after 350 °C sintering. a** Zn edge X-ray absorption spectrum near edge structure (XANES) and **b** correspondent phase-uncorrected moduli of the Fourier transform results. **c** Pb edge X-ray absorption spectrum near edge structure (XANES) and **d** correspondent phase-uncorrected moduli of the Fourier transform results.

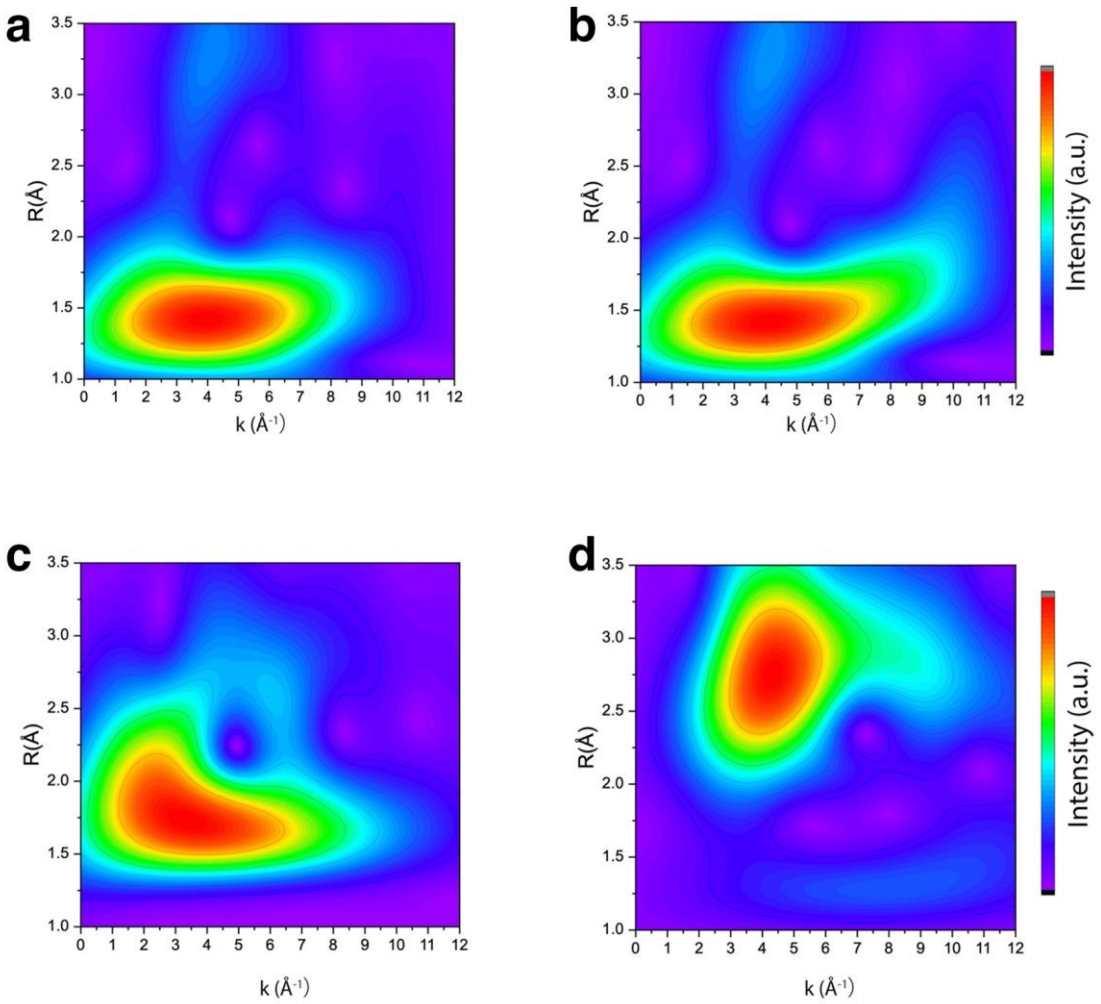


**Supplementary Fig. 30.** Full-range wavelet transform representation of the EXAFS signal for the $(CsPbI_3)_{0.25}(a_gZIF\text{-}62)_{0.75}$ composites. **a** Zn and **c** Pb represent the sample prior to sintering, and **b** Zn and **d** Pb represent the sample after 350 °C sintering.

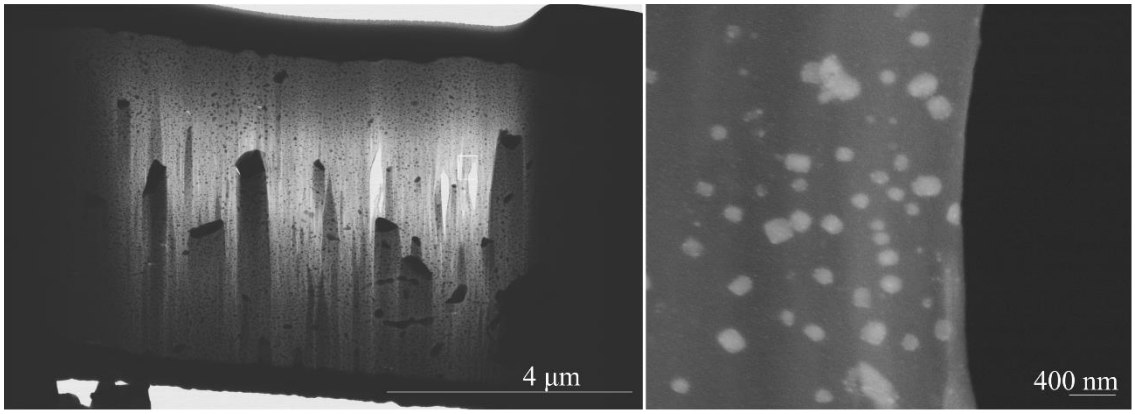


**Supplementary Fig. 31. FIB-SEM images for $(CsPbI_3)_{0.25}(a_gZIF\text{-}62)_{0.75}$ composites sintering 350 °C.**

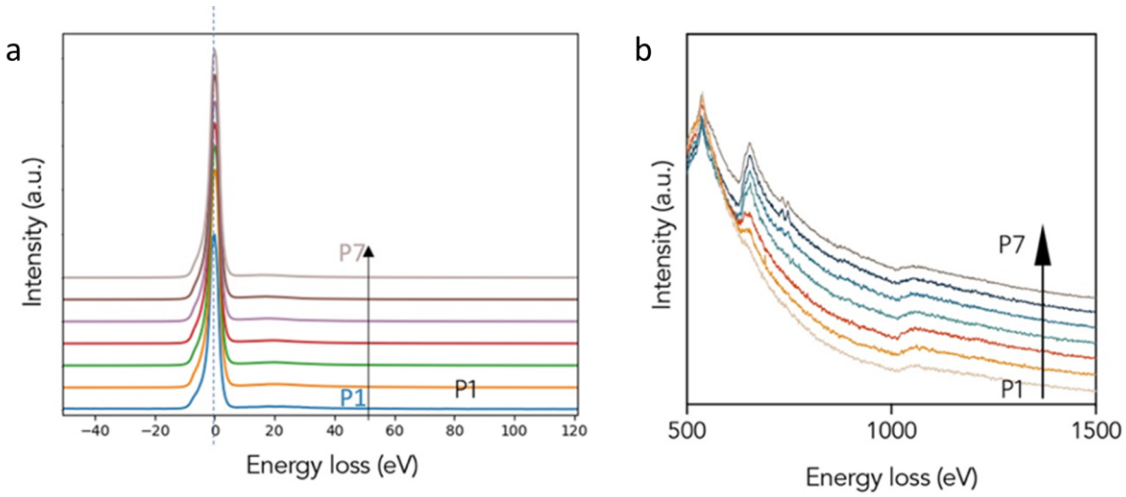


**Supplementary Fig. 32. Data processing to for the TEM-EELS results of $(CsPbI_3)_{0.1}(agZIF\text{-}62)_{0.9}$ composites sintered at 350 °C. a** Zero loss peak: normalised to total low loss scattering (plot with Y-offsets) and **b** Core loss: Normalised to total core loss scattering (plot with Y-offsets)

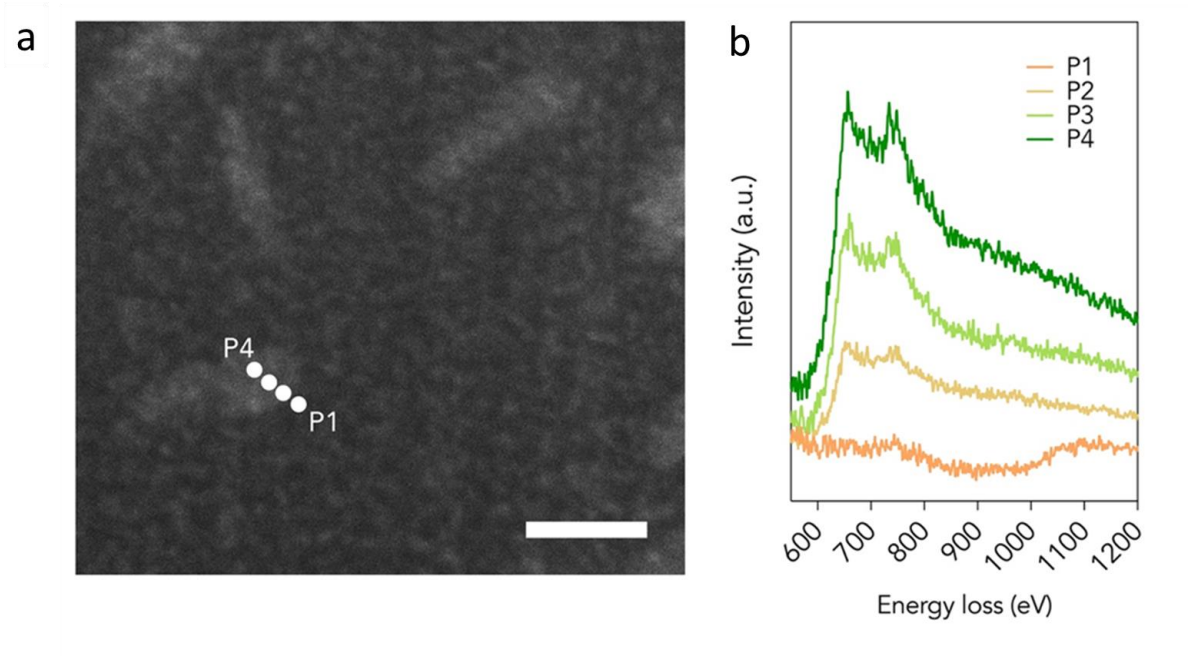


**Supplementary Fig. 33. a Bright field STEM image of $(CsPbI_3)_{0.1}(a_gZIF\text{-}62)_{0.9}$ composites sintered at 275 ℃. Scale bar, 50 nm. b EELS spectrum acquired from the marked points shown in TEM image.**

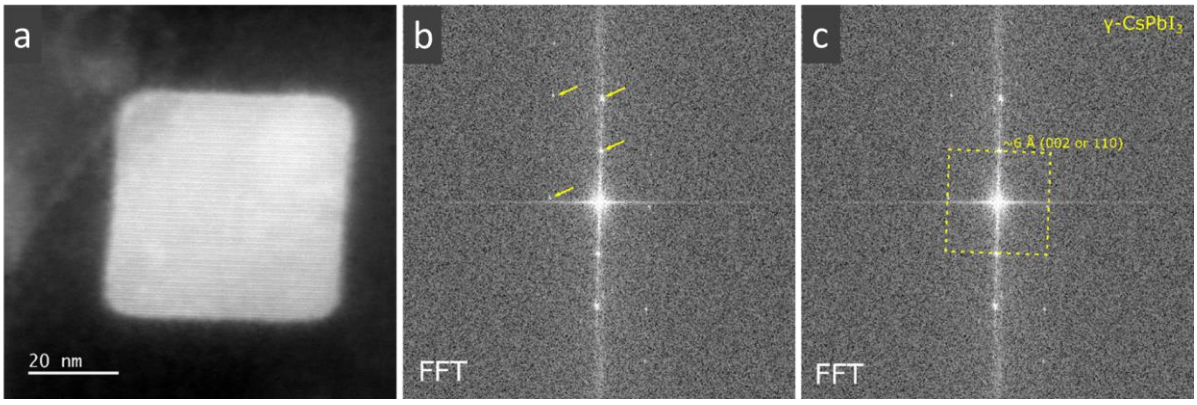


**Supplementary Fig. 34. a** Lattice-resolved ADF-STEM image of a FIB lamella showing a $CsPbI_3$ nanocrystal in $a_g$ZIF-62. **b, c** The fast Fourier transform (FFT) of the crystal image was indexed to γ-$CsPbI_3$ based on the approximately square pattern of spots at ~6 Å (real-space spatial frequency). Annotations in yellow highlight the position of spots and their approximately square symmetry.

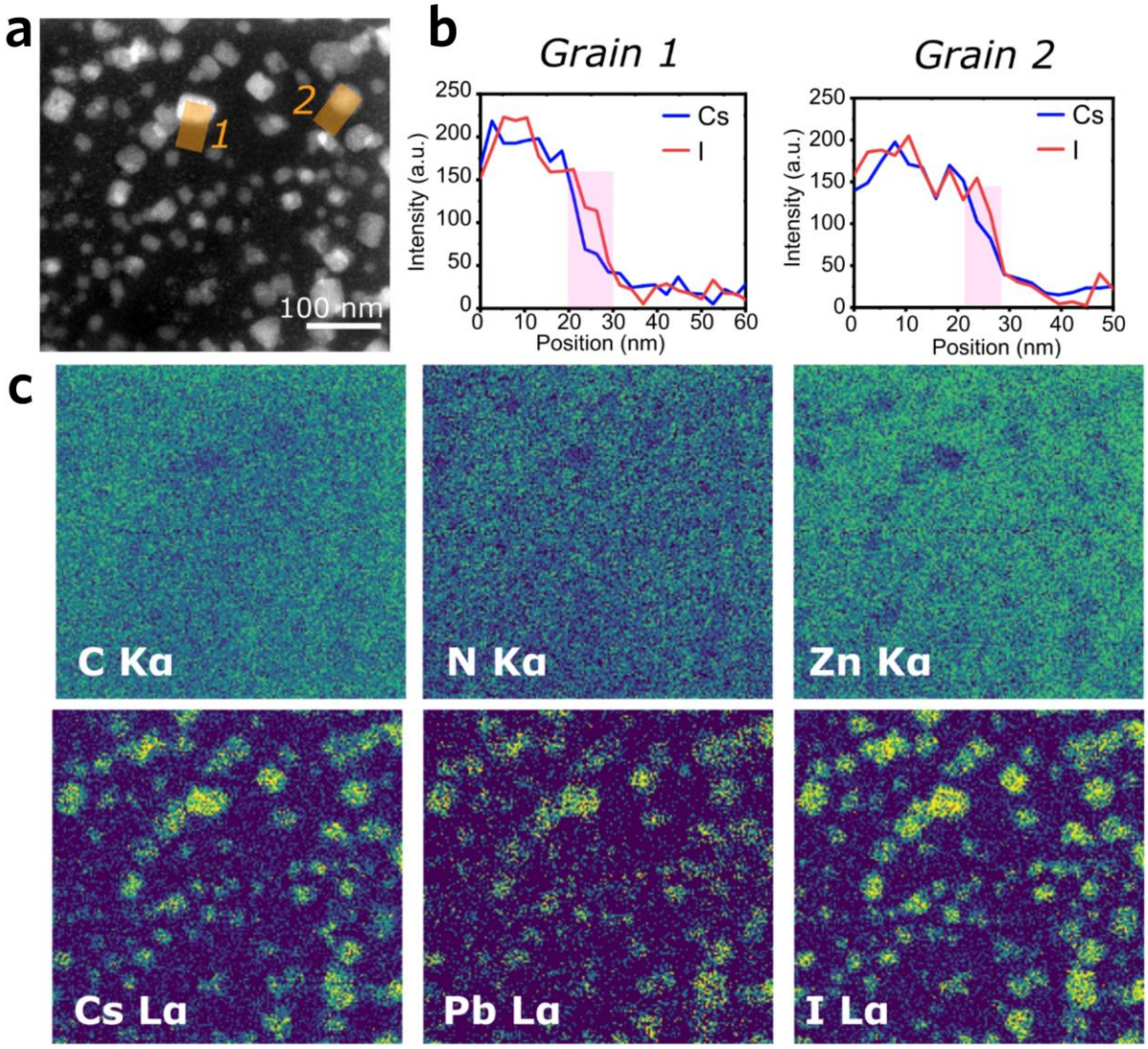


**Supplementary Fig. 35. STEM-EDS analysis of $CsPbI_3$ nanocrystals in $a_g$ZIF-62. a** An overview ADF-STEM micrograph and **b** corresponding line profiles marked in orange. The line profiles show the Cs Lα and I Lα X-ray intensity at selected grains. The I Lα intensity extends further with the Cs Lα intensity decaying faster (magenta shaded regions), corroborating the ~5-10 nm further extension of I intensity observed in EELS beyond the detection of Cs in the nanocrystals. **c** EDS maps showing the major constituents of $a_g$ZIF-62 (C, N, Zn) and $CsPbI_3$.

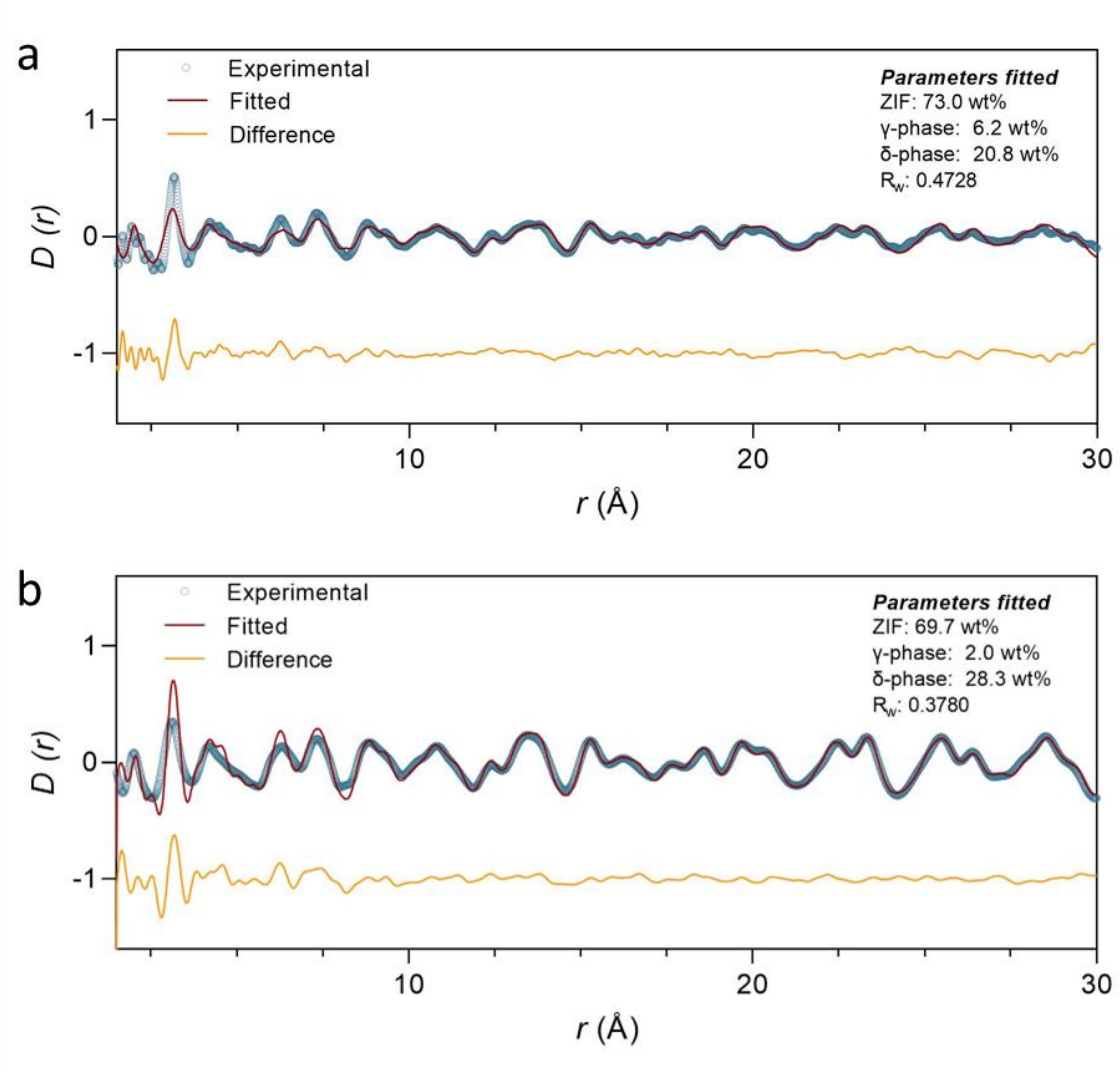


**Supplementary Fig. 36.** Atomic pair distribution functions for $(CsPbI_3)_{0.40}(a_gZIF\text{-}62)_{0.60}$ composites sintered at **a** 325 and **b** 350 °C. Pair distribution function *D(r)* calculated *via* Fourier transform of the X-ray total scattering function.

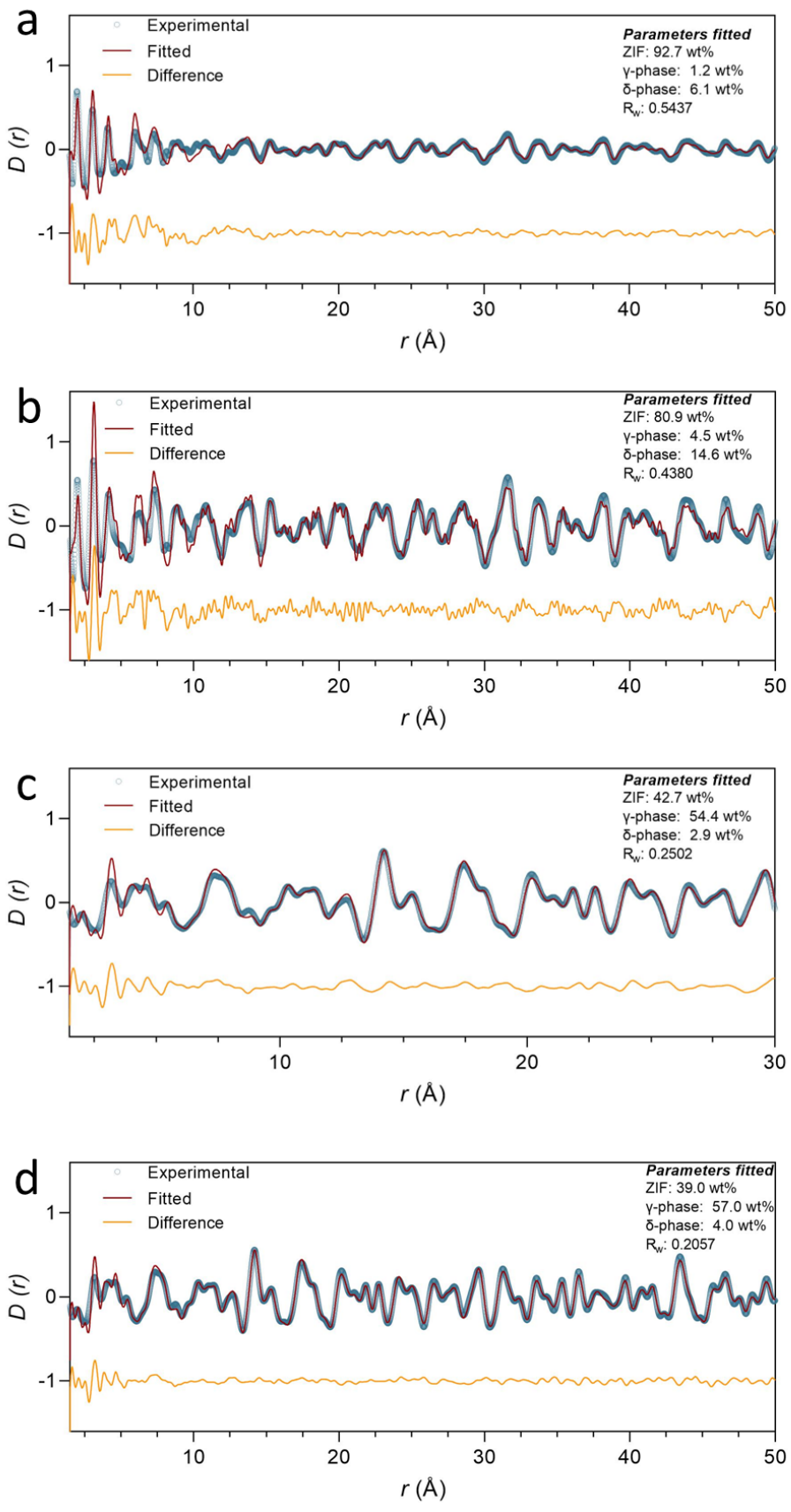


**Supplementary Fig. 37.** Atomic pair distribution functions for composite sintered at 350 °C with different $CsPbI_3$ loadings. **a** 10 wt%, **b** 25 wt%, **c** 70 wt% and **d** 85 wt%.

## Supplementary References


1 Marronnier, A. *et al.* Anharmonicity and Disorder in the Black Phases of Cesium Lead Iodide Used for Stable Inorganic Perovskite Solar Cells. *ACS Nano* **12**, 3477-3486 (2018).

2 Hou, J. *et al.* Halogenated Metal-Organic Framework Glasses and Liquids. *J Am Chem Soc* **142**, 3880-3890 (2020).